

Lead convection measured with an autonomous underwater vehicle

James H. Morison

Polar Science Center, Applied Physics Laboratory, University of Washington, Seattle

Miles G. McPhee

McPhee Research Company, Naches, Washington

Abstract. The winter Lead Experiment (LeadEx) was conducted during 1992 in the Beaufort Sea. There the Autonomous Conductivity Temperature Vehicle (ACTV) was operated under and around leads. These are the first measurements of this kind. Measurements of temperature, salinity, and turbulence parameters were also made at lead edges with sensors fixed to rigid masts. By combining information from the fixed measurements and the ACTV an inertial dissipation method is used to derive horizontal profiles of salt flux from ACTV salinity measurements. Comparisons also show that turbulent vertical velocity perturbations can be estimated from the vertical motion of the ACTV. With these velocity estimates, horizontal profiles of the turbulent fluxes of heat, $w'T'$, and salt, $w'S'$, are also computed directly. Data from a wide (1000-m-wide) lead with rapid ice motion indicate stronger turbulence under the lead than downstream, but the character of the flow is that of a convective boundary layer modified by a change in surface buoyancy flux. The convection is characterized by multiple, intermittent plumes that scale in size with the mixed layer depth. At a medium-sized (100-m-wide) lead with slower ice motion the convective circulation set up by the lead is more apparent. Convective plumes are stronger and more prevalent at the lead edges, particularly the downstream edge. The comparison between the horizontal profiles from the ACTV and time series from fixed sensors suggests that lead convection is a combination of a near surface convective boundary layer and a deeper quasi-stationary convection pattern.

1. Introduction

Convection under winter leads has an important impact on the upper layers of ice-covered seas. The buoyancy flux, which along with surface stress controls the mixed layer, is mostly concentrated in the relatively narrow strips beneath leads. *Maykut* [1978] has suggested that open leads, thin ice, and thick ice contribute about equally to the total heat flux and ice formation. Because of the relatively small fraction of the surface area occupied by leads this indicates that the salt flux, and consequently the buoyancy flux at the ocean surface, is concentrated in narrow bands. In this respect, ice-covered waters are different from ice-free waters where the distribution of surface fluxes is relatively uniform.

The effect of the concentrated buoyancy flux on mixed layer dynamics must depend on the circulation pattern set up by the convection. *Morison et al.* [1992] examined historical data to get some idea of the oceanographic effects of winter leads. The historical observations show a pattern of velocity jets toward the leads just under the ice and salinity disturbances and out-flowing jets at the base of the mixed layer and in the pycnocline. Most of these observations were made under calm conditions. They suggest a cellular convection pattern under the lead as first described by *Smith* [1973]. The underlying idea is that a steady circulation due to the lead is superimposed on the normal under-ice flow pattern. *Morison et al.* [1992] argue that

lead convection typically falls between extremes of free and forced convection. Free convection occurs when the ice moves very slowly over the ocean, and the salt flux at the freezing lead surface sets up a convective cell. The salt-rich water at the lead surface, being heavier than the surrounding water, sinks under the lead and flows away from it at the base of the mixed layer. Ambient water flows in toward the lead near the surface. Forced convection occurs when the ice velocity is high. Then strong, turbulence-induced surface stress mixes the salt into the water rapidly enough to prevent the density disturbance and pressure gradients necessary for cellular convection. *Morison et al.* [1992] define a lead number as the ratio between the pressure gradient and turbulent stress terms in the momentum equation and indicate that this ratio will roughly determine which of the two types of convection will dominate the circulation near the lead. A similar nondimensional quantity is the ratio of shear production and buoyant production in the turbulent kinetic energy equation. Both nondimensional numbers are near 1 for medium ice speeds and typical air temperatures, suggesting lead convection will often be a mix of free and forced regimes.

Implicit in the arguments of *Morison et al.* [1992] are the ideas that the free convection pattern will have a horizontal scale similar to the lead width and that the forced convection pattern will blend the added salt smoothly into the mixed layer. These ideas were based on the original concept proposed by *Smith* [1973] and others. *Schaus and Galt* [1973] describe a lead model based on boundary layer modification or forced convection. *Kozo* [1983] presents the first lead model that at

Copyright 1998 by the American Geophysical Union.

Paper number 97JC02264.
0148-0227/98/97JC-02264\$09.00

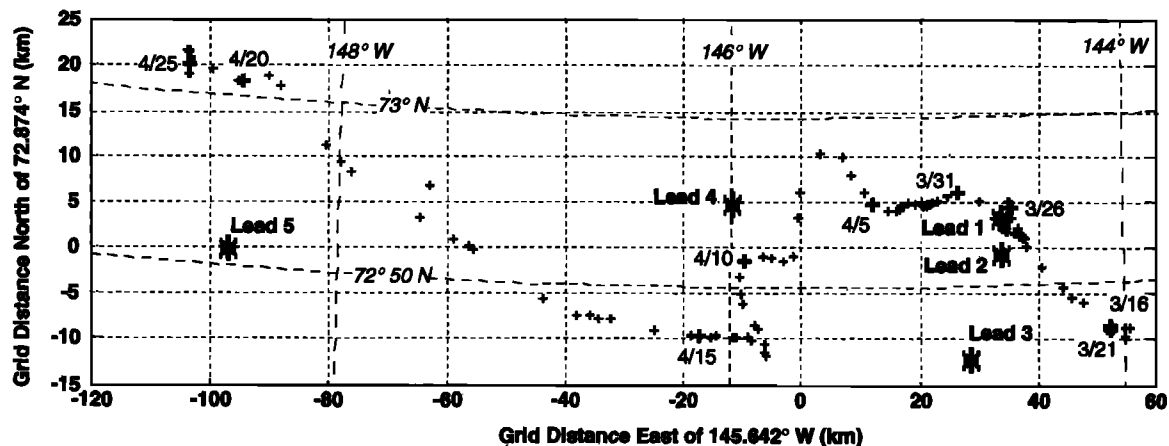


Figure 1. The Lead Experiment (LeadEx) base camp positions (crosses) and lead sites (asterisks) from Camp Manager's log. The dates are month and day of 1992.

tempts to include the effects of turbulence and pressure gradients due to buoyancy flux. Although computational power severely limited the simulation time, Kozo produced a steady, plume-like convection superimposed on a mean boundary layer flow. Kantha [1995] used a higher-order closure [Mellor and Yamada, 1982], which produced a dominant, steady plume under the downstream edge of the lead. The plume persisted for several days. Smith and Morison [1993] used a simpler parameterization of turbulent diffusion; the turbulent diffusion under the lead was restrained to the maximum value occurring under solid ice upstream of the lead, resulting in a different picture from that of Kozo [1983] and Kantha [1995]. Their model produced multiple cells which scaled with the mixed layer depth and were often concentrated at the two lead edges. The plumes were episodic, appearing and disappearing on timescales of 1–2 hours. For intermediate ice speeds the modeled plumes became drawn out and diffused more rapidly, but in many respects they appeared similar to the free convection plumes.

While horizontal variations are intrinsic to lead convection, there have been no detailed observations of horizontal variability until now. Solid sea ice makes such measurements difficult except in the context of fixed-point arrays. The presence of new lead ice, too thick to navigate and too thin to walk on, makes even this type of measurement difficult. The work reported here addresses the problem by means of an autonomous underwater vehicle called the Autonomous Conductivity Temperature Vehicle (ACTV). It was used to measure horizontal variability as part of the Lead Experiment (LeadEx) sponsored by the Office of Naval Research. To our knowledge, these are the first measurements of this kind. The vehicle measurements combined with time series observations of turbulence at the lead edges suggest that the spatial scale of the lead and vertical development of the convective boundary layer are important in determining the pattern of lead convection. They also show that aspects of both boundary layer convection and quasi-stationary cellular convection may appear at the same lead.

2. LeadEx and the ACTV

The main LeadEx field program began on March 16, 1992 [LeadEx Group, 1993]. The approach was to construct a base camp on the ice pack, from which an area 32 km in radius

around the central site was searched daily for fresh leads. With the discovery of a suitable lead, 10 lightweight huts containing the instrumentation were lifted by helicopter to the site. A small pilot experiment in April 1991 served to test a number of new measurement techniques and demonstrate the feasibility of the operational approach. The main experiment base camp was established at 72°47'N, 144°W on March 12, 1992. As shown in the plot of daily positions in Figure 1, the camp drifted generally westward until the program ended on April 25, 1992, at 73°3'N, 148°25'W. Deployments were made from the base camp to four leads. The first two sites closed soon after being occupied, and most of the lead data were gathered at leads 3 and 4. High winds prevented moving huts to lead 5, but a small subset of data was gathered there.

Figure 2 illustrates the arrangement of the ACTV and fixed-point turbulence instrumentation at lead 3. The arrangement at lead 4 was similar. Huts for the operation of these instruments were positioned with most of the other instruments on the upwind edges of the leads. Since ice typically drifts downwind relative to the underlying water, the upwind edge of the ice is usually downstream with respect to currents observed in a reference frame attached to the ice. Time series of turbulence data were gathered with turbulence instrument clusters (TICs) mounted on a rigid mast that could be lowered as a unit to any level in the mixed layer. The mast was installed through a hole about 3 m from the lead edge, and the hut containing the recording system was positioned nearby. Each TIC included three small ducted current meters oriented along mutually orthogonal axes canted 45° to the horizontal. A fast response thermometer (Sea-Bird Electronics SBE-3) and ducted conductivity sensor (SBE-4) were mounted very close to the current-sensing triplet to complete the TIC. The basic system and its capacity to measure heat and momentum fluxes in the neutrally stratified boundary layer are described by McPhee [1992]. Four clusters were used on the mast, with clusters 2, 3, and 4 being positioned 1, 3, and 6 m below the top cluster. The mast was equipped with a vane to align the sensors into the mean flow, and the mast's orientation was monitored with a fluxgate compass, tiltmeters, and a pressure sensor. The response of the ducted cell is limited at wavelengths shorter than about 3 m, tending to degrade estimates of salinity flux [McPhee and Stanton, 1996]. On cluster 2 the standard ducted conductivity cell was replaced with a microstructure conduc-

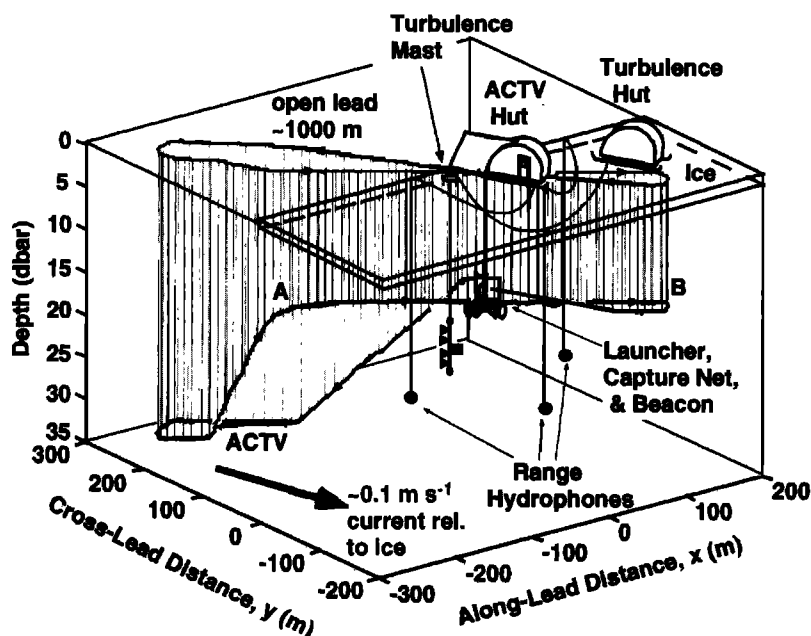


Figure 2. Typical Autonomous Conductivity Temperature Vehicle (ACTV) setup and run during LeadEx. This shows run 5 at lead 3 in a perspective view. The run trajectory is projected on the upper surface, and the vehicle depth is shown as the bottom of a curtain hanging from the trajectory. The surface equipment is shown for the ACTV and fixed-mast turbulence measurements. The ACTV equipment includes the ACTV, the hut from which the vehicle was deployed and recovered, the homing beacon, and the acoustic tracking range. The locations of the tracking hydrophones and ACTV launch point are drawn to scale. The mast with the turbulence sensors is in the correct relative position but was actually 7 m from the launch point and 3 m from the lead edge. The huts are not drawn to scale.

tivity meter (SBE-7). Although lacking the long-term stability of the SBE-4, this dual electrode cell resolves wavelengths through the inertial subrange. This provides more accurate estimates of salinity flux than the SBE-4.

The ACTV (Figure 3) has been developed at the Applied Physics Laboratory, University of Washington. It weighs 10 kg in air, is 1.6 m long and 0.09 m diameter, and is capable of over 1 hour of operation at speeds of nearly 2 m s^{-1} and depths of

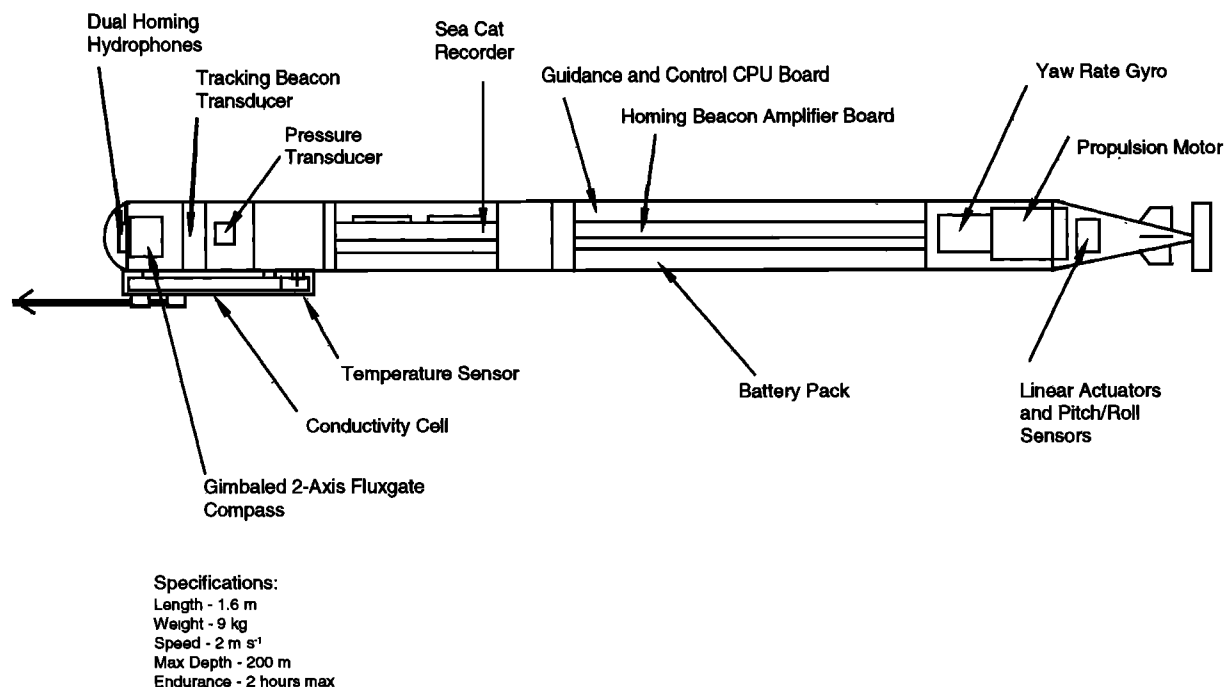


Figure 3. ACTV configuration showing the layout of the sensors, recorder, and control system.

Table 1. LeadEx ACTV Run Summary

Run	Date	Time, UTC	Duration, s	Depth, m	Pattern	Reattacks	Frame TIC Depth
<i>Lead 2</i>							
1	March 29	2301	375	23	front hairpin	0	
2	March 30	0127	402	14	back hairpin	0	
3	March 30	0300	855	5	racetrack, no record	1	
<i>Lead 3</i>							
1	April 7	0333	605	14	front hairpin	0	
2	April 7	0452	809	16	figure eight, miss	1	9.3
3	April 7	1951	855	8	figure eight	1	13.8
4	April 7	2235	822	15	figure eight	0	13.8
5	April 8	0113	773	33 and 15	figure eight	0	
6	April 8	1830	497	17	front hairpin	0	
7	April 8	2310	1122	16	front hairpin, miss	3	
8	April 9	0118	784	9	front hairpin, miss	2	
9	April 9	0322	1315	33 and 15	figure eight, miss	3	
<i>Lead 4</i>							
1	April 12	0241	1343	15	figure eight	1	
2	April 12	0516	776	9	figure eight	0	
3	April 12	0626	831	9	racetrack, down lead	1	
4	April 12	2154	1175	9 and 15	figure eight	2	
5	April 12	2316	650	9 and 15	racetrack	0	
6	April 13	0034	743	6, 9, and 15	racetrack	0	
7	April 13	0217	651	9 and 15	racetrack	0	
8	April 13	0434	581	5 and 15	racetrack	0	

up to 200 m [Morison, 1989; Light and Morison, 1989]. It is equipped with a Sea-Bird Electronics SeaCat conductivity-temperature-depth (CTD) system modified to take data at 9 Hz with 16-bit resolution. The vehicle can be programmed to run a dead-reckoned course and then home on an acoustic beacon. Its position is tracked within an uncertainty of 1–2% with a portable acoustic tracking range.

The ACTV operation at a typical lead is illustrated in Figure 2. The order of deploying the ACTV was to move the hut near the lead and extend a vestibule out over the lead edge. Three hydrophones for the acoustic tracking range were set out, two at the lead edge 100 m on either side of the launch hut and one 100 m back from the lead edge, all at 25 m depth. An acoustic homing beacon and recovery net were suspended below the hut vestibule. A typical vehicle run started with launch from a special fixture lowered down the homing beacon cable. In run 5 at lead 3, illustrated here, the ACTV was lowered to about 15 m. The vehicle run program started once the vehicle was lowered past a preset turn-on depth. After an interval of 45 s the propulsion motor turned on, and the vehicle was released from the launcher. It then executed a programmed, dead-reckoned run pattern. In this case the ACTV dove to 35 m, went upstream about 350 m, turned around, and climbed to 15 m (point A in Figure 2). Most of the return run downstream was at 15 m. After continuing under the ice the vehicle turned back (point B) toward the hut. At this point the vehicle went into a homing mode, returned to the beacon, and was captured in the recovery net positioned slightly above the homing beacon. A small barb on the front of the ACTV tangled in the net to achieve capture.

The quality of the ACTV CTD data is quite good [Light and Morison, 1989]. The sensor manufacturer advertises absolute accuracies of 0.01°C and 0.001 S m⁻¹ or better. However, our experience is that with careful in situ intercalibration, different Sea-Bird sensors agree to better than 0.001°C and 0.001 practical salinity units (psu) over periods of days. For our purposes the ability to detect fluctuations is most important. In what

follows we will show that the ACTV resolves signals much smaller than 0.001°C and 0.001 psu. The digitizing resolution is smaller than 0.0001°C and 0.0001 psu. In describing the results we will also show that the spatial resolution is adequate to examine the energy containing scales of turbulence.

During LeadEx, 20 ACTV runs were made: three at lead 2, nine at lead 3, and eight at lead 4. These are listed along with pertinent run data in Table 1.

3. Convection Under a Lead With Rapid Ice Motion

3.1. Basic Observations

Lead 3 was occupied from April 6 to April 9, 1992, near 72°45'N, 144°50'W. At the deployment site it was about a kilometer wide and was oriented east-west. The mixed layer depth, d , was about 30 m [Muench *et al.*, 1995]. The velocity of the ice, U_i , relative to the water was typically about 0.11–0.13 m s⁻¹ toward the southeast.

A sample of data in Figure 4 from the fixed mast at the edge of the lead illustrates some of the key features of the boundary layer observed in the conventional way. Figure 4 is taken from Figure 2 of McPhee and Stanton [1996]. Note that in this figure, and McPhee and Stanton [1996] in general, velocities and fluxes are positive upward while the convention for the ACTV data will be velocity and fluxes positive downward. Figure 4 shows the salinity deviation, S' , the temperature deviation, T' , the vertical velocity perturbation, w' , and the instantaneous salt and heat (temperature) fluxes, $w'S'$ and $w'T'$. The parameter w' is characterized by distinct downward pulses at a period of 8–10 min. Assuming that flow features are advected with the mean flow velocity, the pulses are separated by 50–60 m or about twice the mixed layer depth. The S' and T' records are similar to the w' record. This results in a downward salt flux concentrated in narrow plumes about $2d$ apart. A substantial downward heat flux occurs despite freezing at the surface,

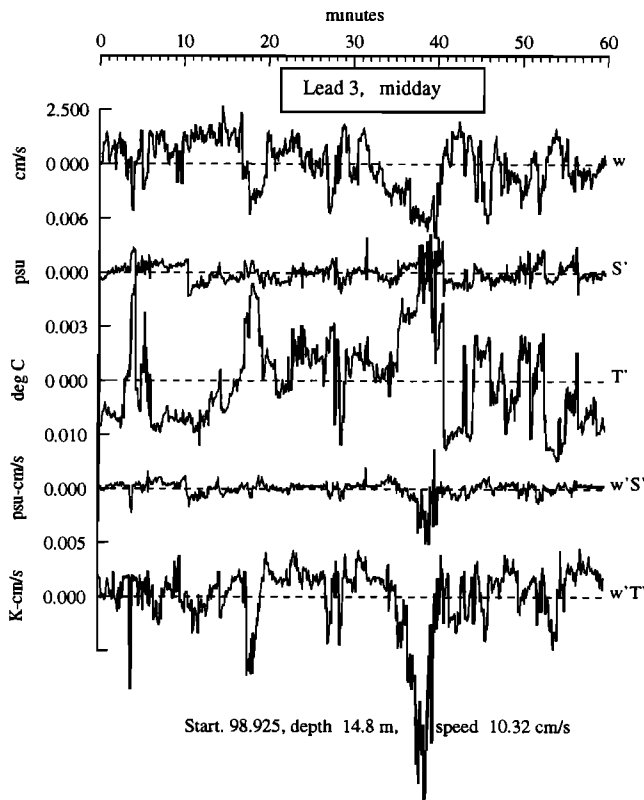


Figure 4. One-hour time series of mast-derived vertical velocity deviation, w' , salinity deviation, S' , and temperature deviation, T' , (linearly detrended) for TIC number 2 at lead 3, day 98 of 1992 at midday. Also shown are the instantaneous salinity flux, $w'S'$, and heat flux, $w'T'$. For this figure (and Figure 12) the velocity and fluxes are positive upward. The convention for the other figures and the ACTV generally is that velocity and fluxes are positive downward. Average values of the fluxes are $\langle w'S' \rangle = -4.87 \times 10^{-6}$ practical salinity units (psu) m s^{-1} and $\langle w'T' \rangle = -1.74 \times 10^{-5}$ K m s^{-1} [from *McPhee and Stanton, 1996*].

owing to downward mixing of solar energy absorbed in the upper few meters under the lead [*McPhee and Stanton, 1996*].

A sample of ACTV data from the portion of run 5 between points A and B in Figure 5 illustrates many of the important features observed with the ACTV. Figure 5a displays the salinity perturbation low-pass filtered with a cutoff frequency of 0.33 cycles per meter (cpm), and the salinity band-pass filtered in a narrow band centered at 0.159 cpm (1 rad m^{-1}). As will be discussed, the variance of the band-passed data represents energy levels in the inertial subrange. The measurements were made at 15 m depth, about middepth in the mixed layer. The salinity record is dominated by substantial peaks at points C and D and a number of less distinct peaks, as at A and B, spaced 50–80 m apart, or slightly over $2d$. The record appears less energetic beyond about 72 m downstream of the lead edge. The salinity perturbations in the larger peaks are about 0.01 psu.

The corresponding temperature record is shown in Figure 5b. The major temperature fluctuations are about 6×10^{-3} °C peak to peak under the lead and about half of that under the ice. High wave number temperature fluctuations with an amplitude of about 10^{-3} °C peak to peak are also apparent. Even the major fluctuations are too small to have a significant effect

on buoyancy compared with the salinity fluctuations, but they are important to the heat flux. The spacing of the major peaks is similar to that for salinity, and there is a weak correlation between salinity and temperature. At B and C the main temperature and salinity peaks are aligned, and near C and A the temperature peaks are slightly upstream of the salinity peaks. The temperature peaks have a ramp-like character, the downstream slope being steeper than the upstream slope. The maxima in the energy of band-passed temperature and salinity appear to be slightly better aligned than the plain temperature and salinity, suggesting a common cause of the variability: turbulent convective plumes.

A comparison of the fixed-mast and vehicle data is illustrated by the plots in Figure 6. These show the average horizontal wave number spectra of salinity (Figure 6a) and temperature (Figure 6b) measured by the two instrument systems during ACTV runs 2–4 at lead 3. During these runs one of the TICs on the mast was at nearly the same depth as the ACTV. Thus, while the measurements are not of the same water, their statistics should be similar. The fixed-mast data are converted to dependence on distance upstream by scaling time with the average water velocity relative to the ice (Taylor's hypothesis). The ACTV and fixed-mast salinity spectra agree to within the confidence limits everywhere except for run 3 at low wave numbers and run 2 at wave numbers greater than 0.2 cpm. The agreement indicates that the ACTV is providing a true measure of turbulent fluctuations and that Taylor's hypothesis applies. The fixed-mast data during runs 3 and 4 show a flattening of the spectral slope between 0.2 and 0.6 cpm, but the data from run 2 do not. *McPhee and Stanton [1996]* attribute this to the competing effects of buoyancy-driven and shear-driven turbulence. The mast salinity roll-off above 0.6 cpm is due to the limited flushing of the SBE-4 conductivity cell in weak currents and does not appear in data from the SBE-7 microconductivity probe mounted at a shallower depth. The ACTV spectra show the same flattening of the spectra starting at about 0.1–0.2 cpm. They flatten even further near 0.05 cpm, where they reach a noise floor at 5×10^{-7} $\text{psu}^2 \text{cpm}^{-1}$. A noise floor at this energy level has been observed in ACTV data from other experiments.

The ACTV temperature spectra of Figure 6b also show good agreement with the fixed-mast spectra. Many of the features are similar to the salinity spectra, especially for runs 3 and 4. For horizontal wave number denoted by k these show a $k^{-5/3}$ wave number dependence. The energy level in run 2 is lower than in runs 3 and 4 because of a difference in radiative heat flux. Runs 3 and 4 were made near midday, when a significant downward heat flux prevailed due to solar radiation entering the lead surface [*McPhee and Stanton, 1996*]. Run 2 was made in the evening, when there was no radiative heating. The ACTV temperature noise floor at 2×10^{-7} $^{\circ}\text{C}^2 \text{cpm}^{-1}$ is apparent in all three runs.

All the spectra show an approximate $k^{-5/3}$ wave number dependence corresponding to the inertial subrange of turbulence. For most runs at LeadEx the ACTV energy is above the noise floor out to about 0.33 cpm. As suggested by *McPhee [1992, this issue]*, we have taken the energy at $k = 0.159$ cpm (1 rad m^{-1}) as a good indicator of the energy in the inertial subrange. It is high enough to give good statistical significance when averaged over scales much smaller than the scale of the lead and mixed layer, and it is low enough to be unaffected by noise floor of the ACTV. Therefore we use the variance of

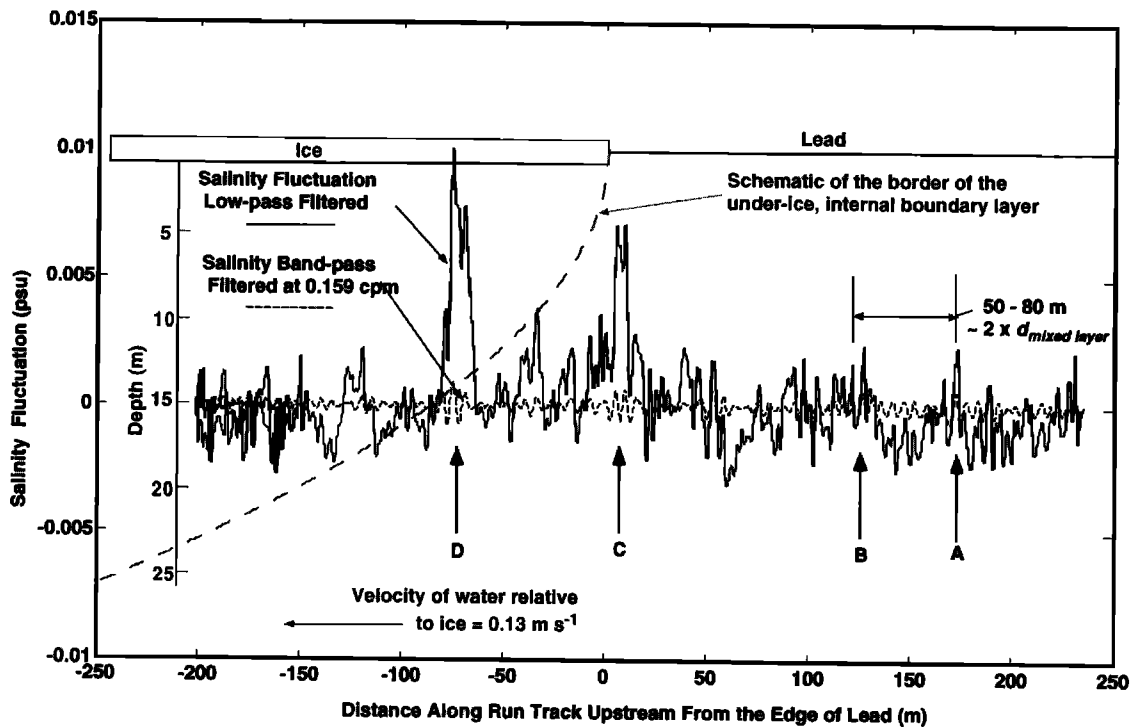


Figure 5a. ACTV salinity fluctuation low-pass filtered with cutoff frequency of 0.33 cpm and the salinity band-pass filtered at 1 rad m^{-1} (0.159 cpm) from run 5 at lead 3 of LeadEx. The dashed line suggests the border of the internal boundary layer under the ice.

band-passed salinity at 0.159 cpm as a proxy for turbulent energy.

The average spatial pattern of convection at lead 3 is illustrated by composite averages of the salinity deviation in Figure

7a and the variance of band-passed salinity in Figure 7b. Salinities measured during runs 1–5 are represented. These runs were used because, as will be shown, they were made when convection was vigorous. As indicated in Table 1, run 3 was at

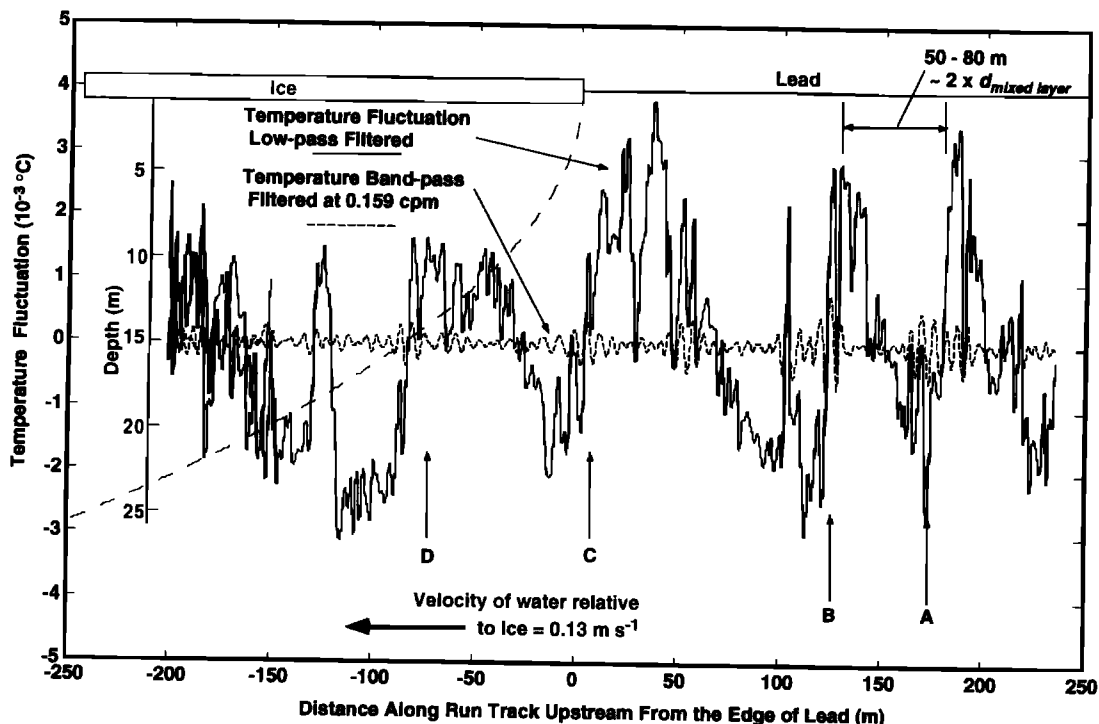


Figure 5b. ACTV temperature fluctuation low-pass filtered with cutoff frequency of 0.33 cpm and the temperature band-pass filtered at 1 rad m^{-1} (0.159 cpm) from run 5 at lead 3 of LeadEx.

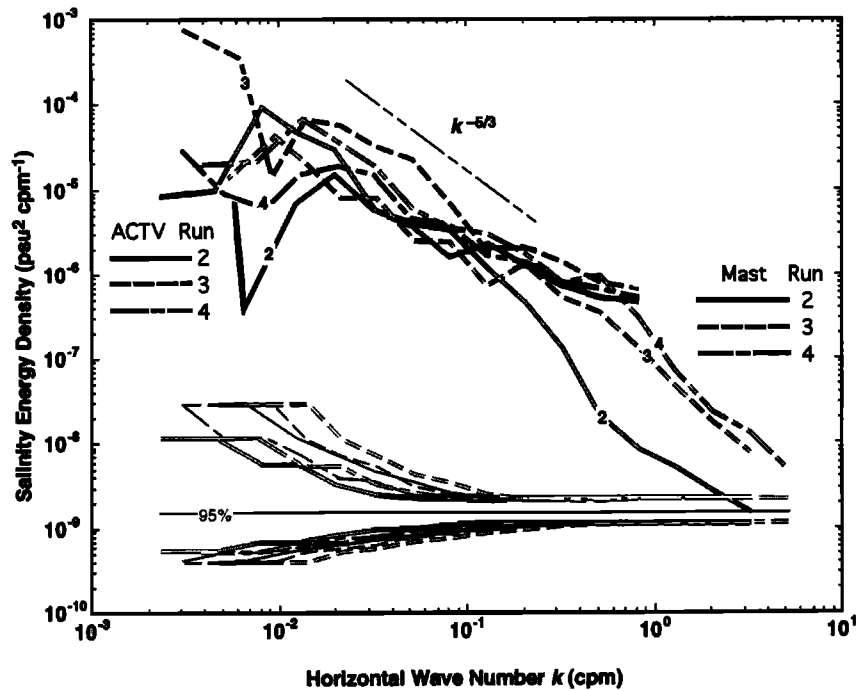


Figure 6a. Mast and ACTV salinity spectra for lead 3, ACTV runs 2, 3, and 4. The mast-derived values are indicated by the white on black lines, and the ACTV values are indicated by black lines. The different runs are indicated by line texture as shown. The confidence limits for each spectrum are also shown in gray with corresponding line patterns.

8 m, and the data from the other runs were gathered at an average depth of 15 m. The data are accumulated and plotted versus distance from the lead edge into the prevailing current at the time of each run. Current directions from the mast data

and the acoustic Doppler current profiler of M. Levine (personal communication, 1993) were used with the ACTV position to determine this coordinate. The salinity deviation is the difference between the measured salinity and a linear fit to

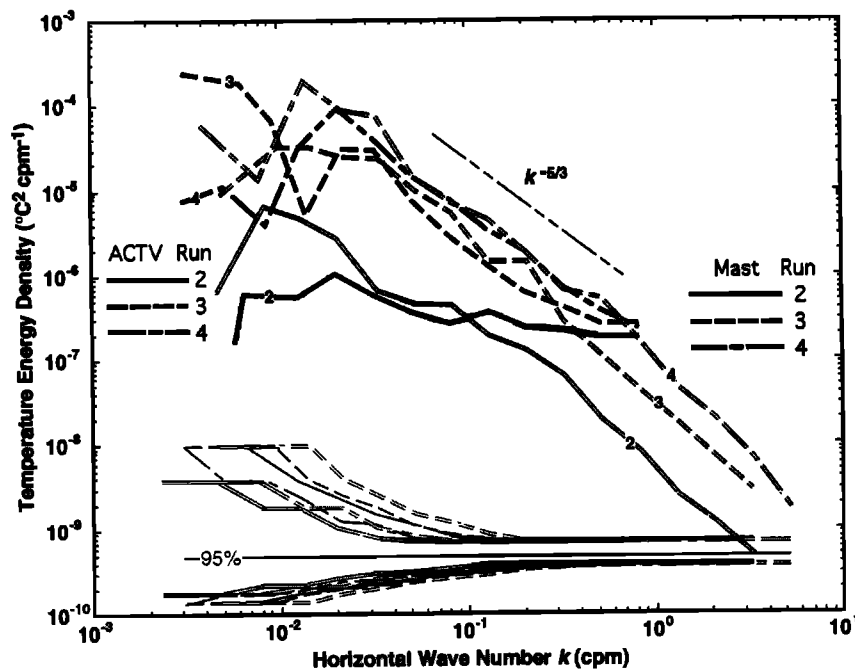


Figure 6b. Mast and ACTV temperature spectra for lead 3, ACTV runs 2, 3, and 4. The mast-derived values are indicated by the white on black lines, and the ACTV values are indicated by black lines. The different runs are indicated by line texture as shown. The confidence limits for each spectrum are also shown in gray with corresponding line patterns.

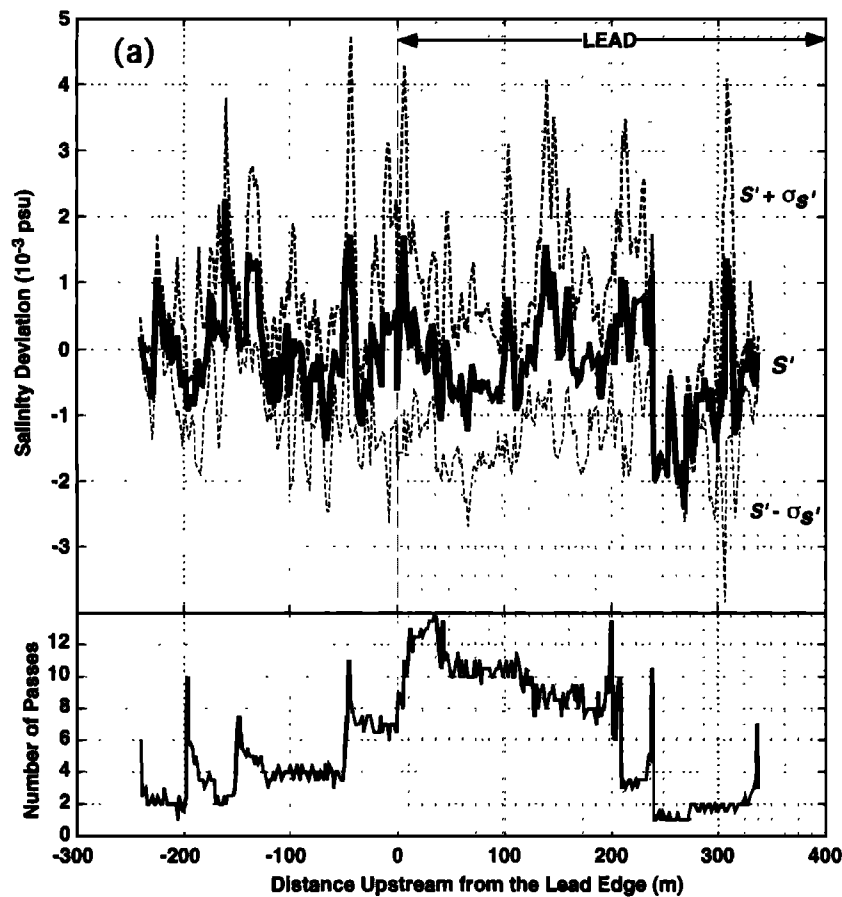


Figure 7a. (top) Composite average of salinity deviation versus upstream distance from the lead edge for ACTV runs 1 to 5 at lead 3. The ± 1 standard deviation error band is also shown. The salinity deviation is computed as described in the text. The results for all runs are collected here in 2-m bins, and (bottom) the equivalent number of ACTV passes through each 2-m bin is shown.

salinity in space and time (of the form $S_0 = A + Bx + Cy + Dz + Et$). This removes any large-scale trends, but at lead 3, where most runs were out and back on a single line, it mainly amounts to detrending the data versus distance from the launch point. A quadratic fit to the first 3 min of each salinity record was also subtracted to account for a startup transient observed in some runs. The results for all runs are collected here in 2-m bins of upstream distance. The salinity composite is shown in Figure 7a (top) and the effective number of ACTV passes through each bin are shown in Figure 7a (bottom). There are about 10 samples per bin per pass. The aim in Figure 7a is to detect any pattern that is tied to the lead geometry. There does not appear to be a strong salinity pattern tied to the lead geometry, but numerous salinity peaks of the order of 10^{-3} psu occur 10–100 m apart.

The variance of band-passed salinity in Figure 7b (top) is more revealing. It is computed by first band-pass filtering the salinity data for each run. This produces a profile such as the band-pass filtered salinity in Figure 5a. The filter has a center frequency of 1 rad m^{-1} and a band width of 0.4 rad m^{-1} . The square of the band-passed salinity is then low-pass filtered with a cutoff frequency of 0.5 rad m^{-1} to remove ripple and yield the running variance of band-passed salinity. Figure 7b (top) is a composite of the variance of band-pass salinity from runs 1 to 5 averaged in 2-m bins. The number of passes through each bin are shown in Figure 7b (bottom). They are slightly different

from those for salinity because variances measured during turns were not used. The variance of band-passed salinity tends to be greater under the lead and drops to lower levels beyond about 72 m downstream of the lead edge. This is mainly apparent in the minima of the variance. The average variance upstream of -72 m is $9.8 \times 10^{-8} \text{ psu}^2$ and downstream it is $6.4 \times 10^{-8} \text{ psu}^2$. This pattern is consistent with a boundary layer response to a decrease in surface flux.

3.2. Salt Flux From the Inertial Dissipation Method

Salt flux is an essential element of lead convection. We can estimate the horizontal variation in salt flux in one way from ACTV salinity because the variance of band-passed salinity can be related to salt flux. This is described in detail in a companion paper by McPhee [this issue]. On the basis of the argument of McPhee [1992] the spectral energy at 1 rad m^{-1} (0.1592 cpm) can be used to characterize the energy in the inertial subrange spectrum. Also, as described by McPhee and Stanton [1996], the inertial dissipation method (IDM) of estimating heat flux [McPhee, 1994] can be applied to estimating turbulent salt flux. Thus horizontal profiles of the variance of band-passed salinity can provide an indirect measure of the horizontal variability of the salt flux. The key equations of the IDM are the turbulent kinetic energy equation and its salinity analog, the salinity variance dissipation equation. An underlying assumption is that the eddy viscosity, K , can be expressed as the

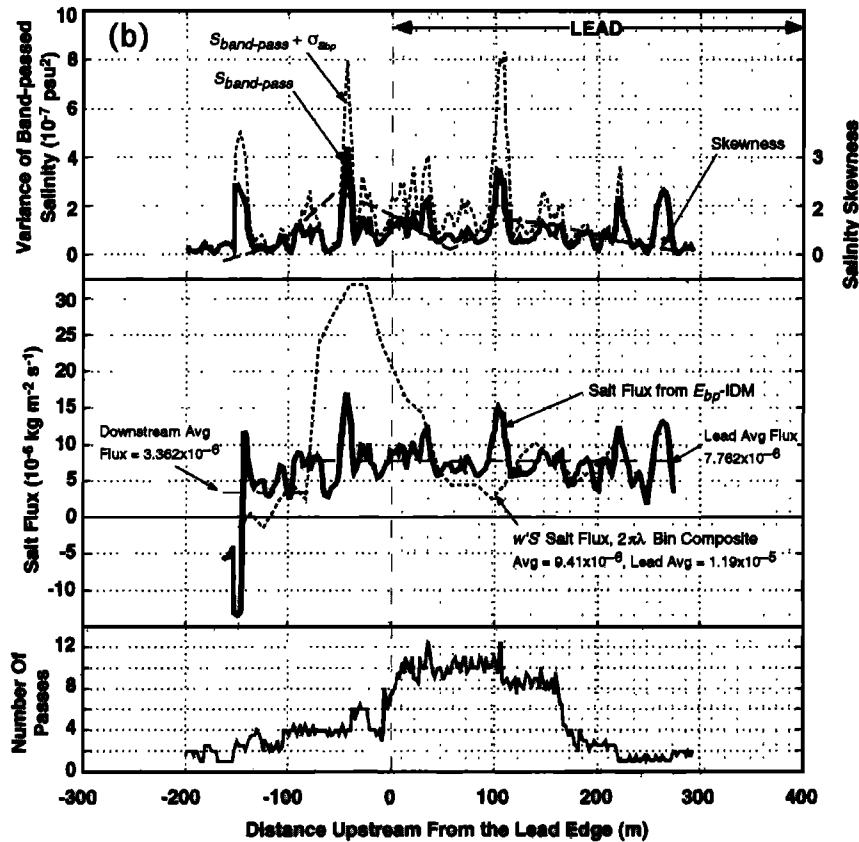


Figure 7b. Composite average of the variance of salinity band-passed at 1 rad m^{-1} for ACTV runs 1 to 5 at lead 3. (top) The average plus 1 standard deviation and the skewness of the salinity perturbation are also shown. (middle) The salt flux estimated using the E_{bp} -IDM method of (7) as described in the text is shown. As in Figure 7a, the results for all runs are collected in 2-m bins of distance upstream from the lead edge, and (bottom) the equivalent number of ACTV passes through each 2-m bin is shown. The variance of band-passed salinity measured during turns is not used. The composite average of ACTV $w'S'$ in $2\pi\lambda$ bins for the same runs is also shown in Figure 7b (middle).

product of the turbulent velocity scale times a mixing length, λ . For neutral stratification the velocity scale is the friction velocity, $u_* = |\langle u'w' \rangle|^{1/2}$, where u' is the downstream velocity perturbation. Thus the local mean shear, $\partial U / \partial z$, can be expressed as u_* divided by λ ,

$$u_*^2 = \langle u'w' \rangle = K \frac{\partial U}{\partial z} = u_* \lambda \frac{\partial U}{\partial z} \Rightarrow \frac{\partial U}{\partial z} = \frac{u_*}{\lambda}. \quad (1)$$

Also, in cases where shear stress dominates buoyancy flux, it is correct to assume dissipation balances shear production in the turbulent kinetic energy equation

$$\left| \langle u'w' \rangle \frac{\partial U}{\partial z} \right| = \frac{\langle u'w' \rangle^2}{\lambda u_*} = \varepsilon. \quad (2)$$

In the salinity equation the production of salinity variance equals the dissipation of salinity variance, ε_s ,

$$\left| \langle w'S' \rangle \frac{\partial S}{\partial z} \right| = \frac{\langle w'S' \rangle^2}{\lambda u_*} = \varepsilon_s. \quad (3)$$

If an inertial subrange exists in the flow, there is a simple relation between the dissipation and the spectral levels at wave numbers within the subrange [Hinze, 1975]. For salinity variance this relation is

$$\varepsilon_s = \frac{\varepsilon^{1/3}}{\alpha_s} S_{ss}(k) k^{5/3}, \quad (4)$$

where S_{ss} is the spectrum and α_s is the Kolmogorov constant for salinity. Combining (2)–(4) yields

$$\langle w'S' \rangle = \frac{\lambda^{1/3} u_*}{\alpha_s^{1/2}} S_{ss}^{1/2} k^{5/6} \quad (5)$$

At lead 3, McPhee and Stanton [1996] found that buoyant production was about equal to shear production away from the ice boundary near the depths of the ACTV runs. Thus (1) and (2) do not strictly apply. However, McPhee and Stanton [1996] also found that at lead 3, away from the ice boundary, $u_* = 0.007 \text{ m s}^{-1}$, $\lambda = 8.9 \text{ m}$, $\varepsilon = 7 \times 10^{-8} \text{ W kg}^{-1}$, and $\alpha_s = 0.98$. These quantities can be used directly with (3) and (4) to yield

$$\langle w'S' \rangle = \left(\frac{\lambda u_* \varepsilon^{1/3}}{\alpha_s} S_{ss} k^{5/3} \right)^{1/2}. \quad (6)$$

The IDM by itself only indicates the magnitude of the flux, not the direction. In a companion paper, McPhee [this issue] shows that the skewness of the scalar distribution is an excellent indicator of the direction of the flux. At lead 3 when the skewness of the mast-measured temperature distribution, η_{tt} ,

was positive, the heat flux was positive downward (day). When the skewness of temperature was negative, the heat flux was upward (night). The skewness of the mast-measured salinity, η_s , was always positive, indicating the salt flux was positive downward. This relation, which is simpler than a similar one put forth by *Thorpe et al.* [1991], is a consequence of the flux being due to strong narrow plumes in the direction of the flux with broader areas of weaker return flow. For example, downward heat flux produces narrow areas of very warm water (moving rapidly downward) and broad areas of slightly cool water (moving slowly upward), resulting in positive temperature skewness. As long as this convective cell geometry applies, the relationship should work.

We can apply the IDM to the ACTV data. We divide the variance of band-passed salinity, E_{bp} , of Figure 7b by the width of the pass band (0.4 rad m^{-1}) to get an effective spectral density at 1 rad m^{-1} and an estimate of the salt flux. With this and an estimate of the skewness the salt flux at lead 3 from the ACTV data is

$$\langle w'S' \rangle = \text{sign}(\eta_s) 0.0256 E_{bp}^{1/2}. \quad (7)$$

In using this relation we assume that the average ϵ , λ , and u_* measured by *McPhee and Stanton* [1996] can be applied everywhere at lead 3. Thus the flux variation is that owing only to the spatial variability of the salinity fluctuations.

The skewnesses for the salinities of Figure 7a were estimated in bins of upstream distance $2\pi\lambda$ wide ($56 \text{ m} \sim 2d$) wide. This was chosen as the smallest width that could sample a complete convective cell. The resulting skewness is shown as a dashed line along with E_{bp} in Figure 7b (top) with the skewness scale axis on the right. The skewness is at least slightly positive everywhere except for the rather poorly sampled region beyond 140 m downstream of the lead.

Figure 7b (middle) shows the average salt flux determined from (7) using E_{bp} and η_s in Figure 7b (top). Recall that our convention in analyzing the ACTV data is that the velocity and fluxes are positive downward. Like E_{bp} the turbulent salt flux is higher under the lead and near the lead edge. It suggests that at the downstream lead edge the boundary layer begins to adjust to a zero flux surface condition. This transition deepens with distance downstream from the edge and reaches 15 m at 70–80 m downstream. The average E_{bp} -IDM salt flux is $0.8 \times 10^{-5} \text{ kg m}^{-2} \text{ s}^{-1}$ under the lead and $0.34 \times 10^{-5} \text{ kg m}^{-2} \text{ s}^{-1}$ beyond 72 m downstream. The peak in flux at 50 m downstream will be discussed in light of other observations.

3.3. Fluxes Estimated Directly From ACTV Data

The direct way to measure turbulent fluxes is to compute the covariance of vertical velocity perturbation and the quantity in question, $\langle w'T' \rangle$ for heat and $\langle w'S' \rangle$ for salt. The ACTV measures T' and S' , and only an estimate of w' is required to make the flux estimates. We have discovered that perturbations in the vertical velocity, w , of the ACTV as measured with its pressure sensor were correlated with energetic salinity disturbances in such a way as to suggest convective plumes and salt flux. With the vehicle programmed to run a level course under leads, downward velocity perturbations corresponded with positive salinity perturbations. These suggest that the vehicle responds to the vertical velocity in the convective plumes. Overall, the data suggest that over length scales of the energy-containing scales of turbulence, the vertical motion of the ACTV can be used as a rough approximation for the turbulent

vertical velocity. This approximation can be used to estimate heat and salt flux. The approach is particularly useful in the study of lead 4. However, lead 3 provides very useful data with which to develop and evaluate the technique because the relative horizontal homogeneity at lead 3 makes it possible to compare the ACTV and mast-derived data. The approach also provides another type of flux measurement at lead 3.

The correlations between the w values of the ACTV and salinity and temperature are statistically significant. To test this, we used the approach of *Fleury and Lueck* [1994]. Two hundred uncorrelated realizations of w , S' , and T' were created for each run at lead 3 by lagging the S' and T' records from lead 3 more than the correlation distance (17.6 m typical) relative to the w record. Figure 8 shows the histograms of the correlation coefficients for all uncorrelated series from runs with covariances $\langle wS' \rangle$ and $\langle wT' \rangle$ greater than $0.25 \times 10^{-5} \text{ (m s}^{-1} \text{ psu and m s}^{-1} \text{ }^\circ\text{C)}$. The normalized means of the correlation coefficients from uncorrelated series are -0.06582 for wS' and -0.01783 for wT' . The true correlations from the unshifted series are also normalized by the run standard deviations and averaged. These are 2.419 for wS' and 2.243 for wT' and are graphed as vertical lines. The true correlation coefficients are 2 orders of magnitude greater than the mean correlations from random series and over 2 times the standard deviation.

The simultaneous fixed-mast and ACTV measurements at lead 3 make it possible to evaluate the magnitude of the ACTV vertical velocity and flux estimates. Figure 9a shows spectra of the turbulent fluctuation in vertical velocity, w' , determined from the fixed-mast and ACTV data gathered during ACTV runs 2–4 at lead 3. Figures 9b and 9c show the spectra of the turbulent salt flux, $w'S'$, and heat (temperature) flux, $w'T'$.

The raw ACTV vertical velocity, w , spectra are shown as thin black lines in Figure 9a. They roughly agree with the fixed-mast w' spectra (white on black lines) in the low-horizontal wave number, high-energy region, but they become higher than the mast-measured spectra starting at about $k = 0.03 \text{ cpm}$. At high wave numbers the ACTV spectra are substantially higher than the mast spectra.

The peak in ACTV velocity at 0.03 cpm may be due to the dynamics of the ACTV. We can imagine that as the vehicle enters a downward plume, it initially tends to pitch downward. This would tend to make the vehicle overrespond to the water motion, but the effect would be reduced as the tail surfaces enter the plume. Of course, the vehicle control system will also tend to return the vehicle to the desired cruise depth if the depth perturbations become large. Usually, the vehicle depth perturbation is small enough that the control system does not cancel out the fundamental plume signal. Thus we see the strong correlation between salinity and ACTV vertical velocity. We think that the surplus of energy at high wave numbers is largely due to least-bit digitization noise and other measurement noise in the pressure data.

An effort has been made to reconcile the ACTV w' estimates so that they more nearly equal the mast-measured w' . The ratio of the mast-derived wave number spectra to the ACTV vertical velocity spectra was calculated as a function of wave number. Linear interpolation was used to account for a slight depth dependence of the mast-measured w' . A phase preserving smoother was then roughly matched to the square root of the ratio and scaled slightly so that the average ratio for the three runs was unity at 1 cycle per 60 m. The smoother was then applied to the ACTV vertical velocity data to yield an

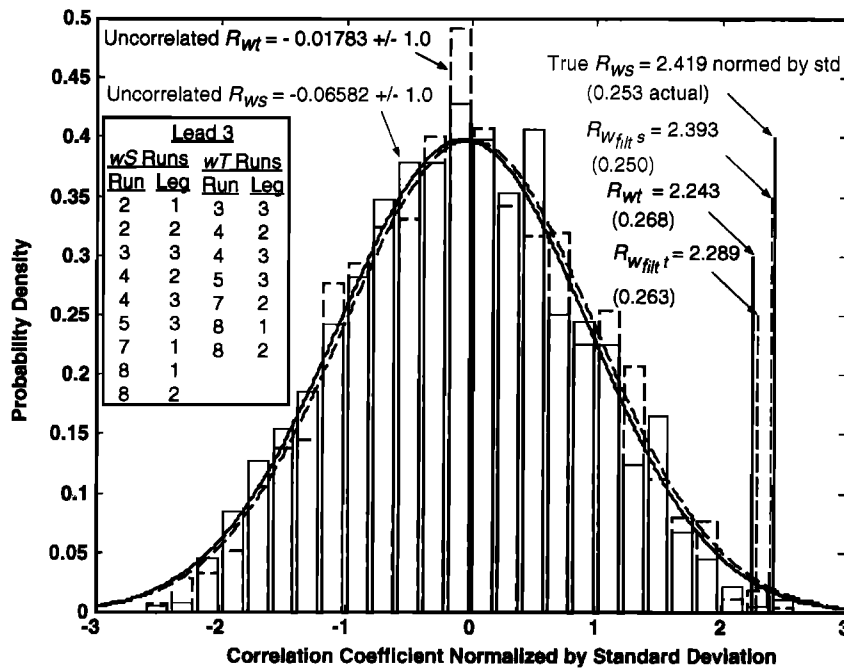


Figure 8. Histograms of correlation coefficient, $R_{ws'}$ and $R_{wT'}$, between uncorrelated ACTV vertical velocity (w) and salinity (S') and temperature (T') series. The series are from runs at lead 3 of LeadEx for which the covariances $\langle wS' \rangle$ and $\langle wT' \rangle$ are greater than 0.25×10^{-5} (m s^{-1} psu and m s^{-1} $^{\circ}\text{C}$, respectively). The run descriptions are given in Table 1, and the method of making the histograms is described in the text. Normal curves have been fitted as shown. The normalized means of the uncorrelated series are -0.06582 for wS' and -0.01783 for wT' . The true correlations from the unshifted series are also normalized by the run standard deviations and averaged. These are 2.419 for wS' and 2.243 for wT' and are graphed as the vertical lines at the right of the plot. Actual average correlations are given in parentheses. The correlations for series with filtered w are also shown.

improved w' estimate. This approach is primitive. However, the results indicate the filtered ACTV w can serve as a useful proxy for the true w' of the water.

The resulting ACTV-derived w' spectra are shown as thick black lines in Figure 9a. The agreement with the mast w' spectra is better than that of the unfiltered ACTV spectra, especially at high wave numbers where the filter works the best. The agreement is good for runs 2 and 4, but the mast-derived energy level for run 3 is substantially lower than the other spectra, especially the ACTV-derived energy for run 3. These differences for run 3 reflect the random nature of the large-scale convective features in the flow. The ACTV and mast spectra for all three runs show an approximate $k^{-5/3}$ dependence above about 5×10^{-2} cpm.

Figure 9b compares the ACTV and mast-derived salt flux spectra. As with the velocity data, the agreement for runs 2 and 4 is reasonable. In fact, the agreement between the salt flux spectra is somewhat better than that for the vertical velocity spectra. This is because the noise in the w' estimate is for the most part uncorrelated with S' . The correlation coefficient between the filtered ACTV w' and S' is over 2 standard deviations from the mean and is only slightly different from that for the unfiltered ACTV w' (see Figure 8). As with w' , the ACTV salt flux spectrum for run 3 is substantially larger than the mast-derived run 3 spectrum. The difference is greater for salt flux because of the low level of salinity fluctuations in the run 3 mast data (Figure 6a).

Figure 9c is a similar comparison for heat flux $w'T'$. Runs 2 and 4 show very good agreement between the ACTV and the

mast spectra. Run 3 shows the relatively low energy but consistent shape measured by the mast. The spectra from both the ACTV and mast are much lower in energy for run 2 than for runs 3 and 4. As mentioned earlier, this is because run 2 was made around dusk, whereas runs 3 and 4 were made around midday the following day. As will be discussed, the radiative heating through the open water and thin ice at the lead surface causes substantial downward heat flux under the lead during the day [McPhee and Stanton, 1996]. For this reason the heat flux during run 2 is substantially lower. Thus Figure 9c illustrates that the ACTV flux estimates are reasonable over a wide range of energy. The heat flux spectra for runs 3 and 4 vary as $k^{-5/3}$ above about 4×10^{-2} cpm. The spectra are much flatter for the low-energy case of run 2.

3.4. Comparison of Lead 3 Flux Estimates

The reasonableness of the flux estimates from the ACTV is further demonstrated by comparing the average fluxes for each ACTV run under lead 3 with flux estimates made by independent means. The comparison also illustrates key findings about lead convection. Figure 10a shows average salt flux estimates derived from ACTV runs 1–9 at lead 3 versus day of 1992. From the ACTV data, S' was combined with w' , estimated as described above, to yield horizontal profiles of $w'S'$ for the straight and level portions of each run. The average flux, $\langle w'S' \rangle$, over the level portions of each run was then computed. These run averages are plotted as individual points at the time of each run. D. K. Perovich and J. A. Richter-Menge (personal communication, 1994) and Perovich *et al.* [1995] have esti-

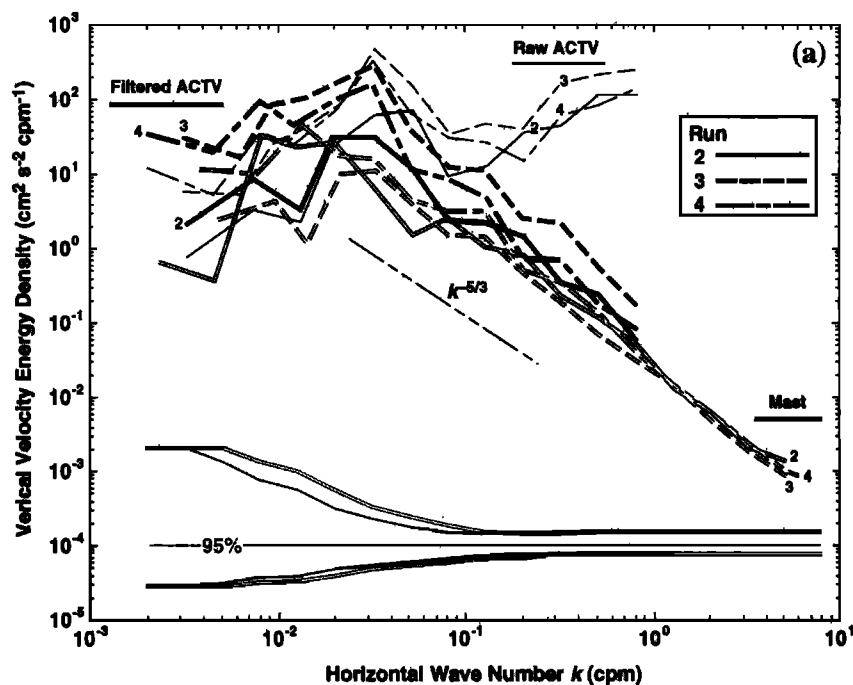


Figure 9a. Mast, raw ACTV, and filtered ACTV vertical velocity spectra for lead 3, runs 2, 3, and 4. The mast-derived values are indicated by the white on black lines, and the ACTV values are indicated by black lines. The different runs are indicated by lines and labels as shown. The average confidence limits for ACTV and mast-derived run spectra are shown in gray. The derivation of the filtered ACTV vertical velocity is described in the text.

mated the salt flux from repeated measurements of ice growth and ice salinity. This is shown by the segmented line. We also show the continuous series of mast-derived measurements of the salt flux at 4 m depth described by *McPhee* [1994]. The

ACTV estimates are within the variability of all the other estimates, and all the data show essentially the same pattern. The ACTV data suggest low fluxes initially, as do the other data. This occurs because the initial ice growth is a matrix of

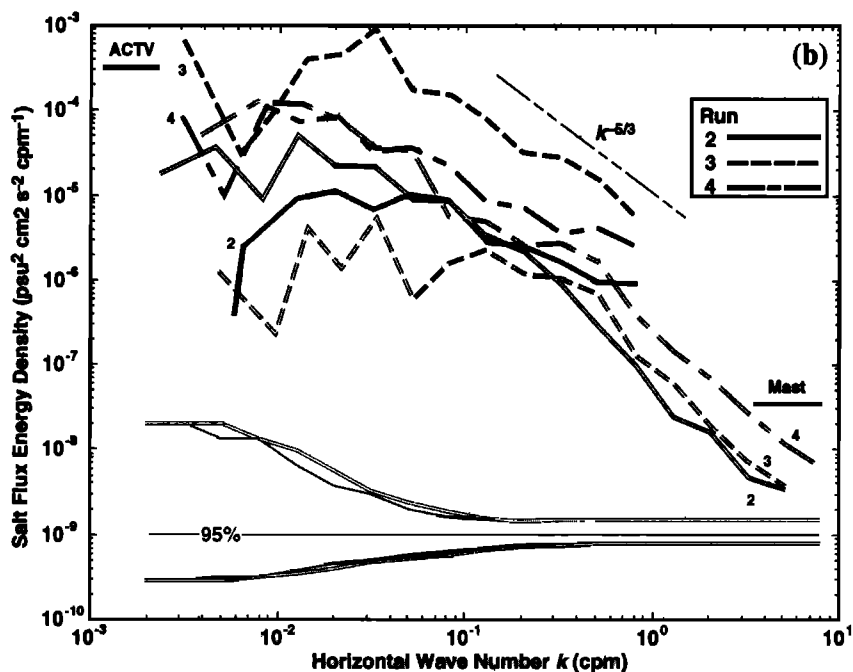


Figure 9b. Mast and ACTV salt flux ($w'S'$) spectra for runs 2, 3, and 4 at lead 3. The mast-derived values are indicated by the white on black lines, and the ACTV values are indicated by black lines. The different runs are indicated by lines and labels as shown. The average confidence limits for ACTV and mast-derived run spectra are shown in gray.

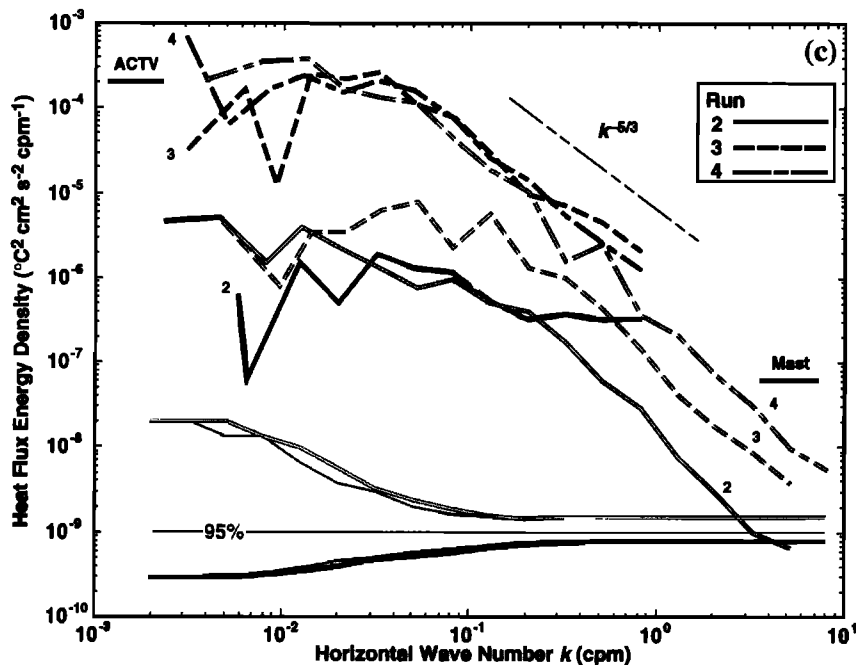


Figure 9c. Mast and ACTV heat flux, $w'T'$, spectra for runs 2, 3, and 4 at lead 3. The mast-derived values are indicated by the white on black lines, and the ACTV values are indicated by black lines. The different runs are indicated by lines and labels as shown. The average confidence limits for ACTV and mast-derived run spectra are shown in gray.

frazil ice which retains brine. Peak fluxes occur after 12–24 hours as indicated by the ACTV data, the *McPhee* [1994] data, and the ice-growth-derived data. This happens after the ice is about 2 cm thick and begins to grow in a columnar structure that allows better brine drainage (J. Wettlaufer, personal communication, 1992). The ACTV and ice data indicate the same low salt flux by day 100 when the ice growth rate has slowed considerably. By this time, turbulent flux levels were too low to be measured with the fixed mast.

The averages of salt flux derived by the E_{bp} -IDM for the runs of Figure 7 are also shown in Figure 10a. The E_{bp} -IDM applied to each run roughly agrees with the run averages of the direct $w'S'$ calculations, but perhaps because temporal variations in the velocity field are not accounted for, E_{bp} -IDM produces less variability than the direct $w'S'$ calculations.

Figure 10b is a plot of the average heat fluxes estimated from the same ACTV runs used in Figure 10a; the measured T' have been combined with w' to produce flux estimates in the way described above for salt flux. The heat flux measurements reported by *McPhee and Stanton* [1996, Figure 11] are shown as solid lines. These were measurements obtained from the fixed mast at 4 m and estimated from dissipation-scale measurements made with a loose-tethered microstructure profiler (LMP). The ACTV results agree well with the heat flux estimated by the other instruments. The *LeadEx Group* [1993] reports that the heat flux exhibited a strong diurnal cycle. During daylight (marked by gray bars in Figure 10b), radiation coming in through the new ice and open water produced heating in the upper few meters of water. This resulted in a net downward heat flux by turbulent mixing. During night the net heat flux was upward because of the sensible heat loss through the thin ice. The ACTV heat flux was maximum downward during full daylight and dropped to low or negative (upward) values during twilight or late afternoon. The ACTV heat fluxes

were lower during the last day, when the ice was thicker and presumably had a higher albedo.

The ACTV is obviously not meant to be a time series instrument. The fluxes under the lead vary considerably in time, as shown by the temporal variation in the fluxes measured by the fixed mast (Figures 6 and 9). They also vary with depth and position. The run-average ACTV fluxes in Figure 10 represent snapshots in time at individual depths from 8 to 17 m and averaged over distances of a few hundred meters each. However, even though the average ACTV fluxes provide only a very sparse time record, they show general agreement with the heat and salt fluxes estimated by other means. This gives us some confidence that the vehicle can extend our turbulence measurements into areas we otherwise cannot reach.

One reviewer expressed surprise that the ACTV motion alone could be used to estimate w' since atmospheric research airplanes require a relative velocity measurement to estimate atmospheric turbulence. This is an issue we are studying, but we think there are several reasons the ACTV and airplanes behave differently. First, the ACTV is neutrally buoyant, while aircraft are supported by aerodynamic lift. In this way the ACTV is essentially a motorized Lagrangian drifter (more analogous to a blimp). The relative vertical water velocity is on average very small and only deviates momentarily when the ACTV is moved into a new updraft or downdraft. If the scale of the updraft is wide enough, the ACTV will move vertically with it as a Lagrangian drifter. Second, the ACTV is slightly unstable, while airplanes are stable. The position and angles of incidence of the wings and horizontal stabilizer of an airplane are set so that an updraft will cause the airplane to pitch down and a downdraft will cause it to pitch up. As a result, an airplane tends to move counter to the vertical air currents, producing large vertical relative air velocities and relatively little vertical airplane motion. Thus much of the signal of

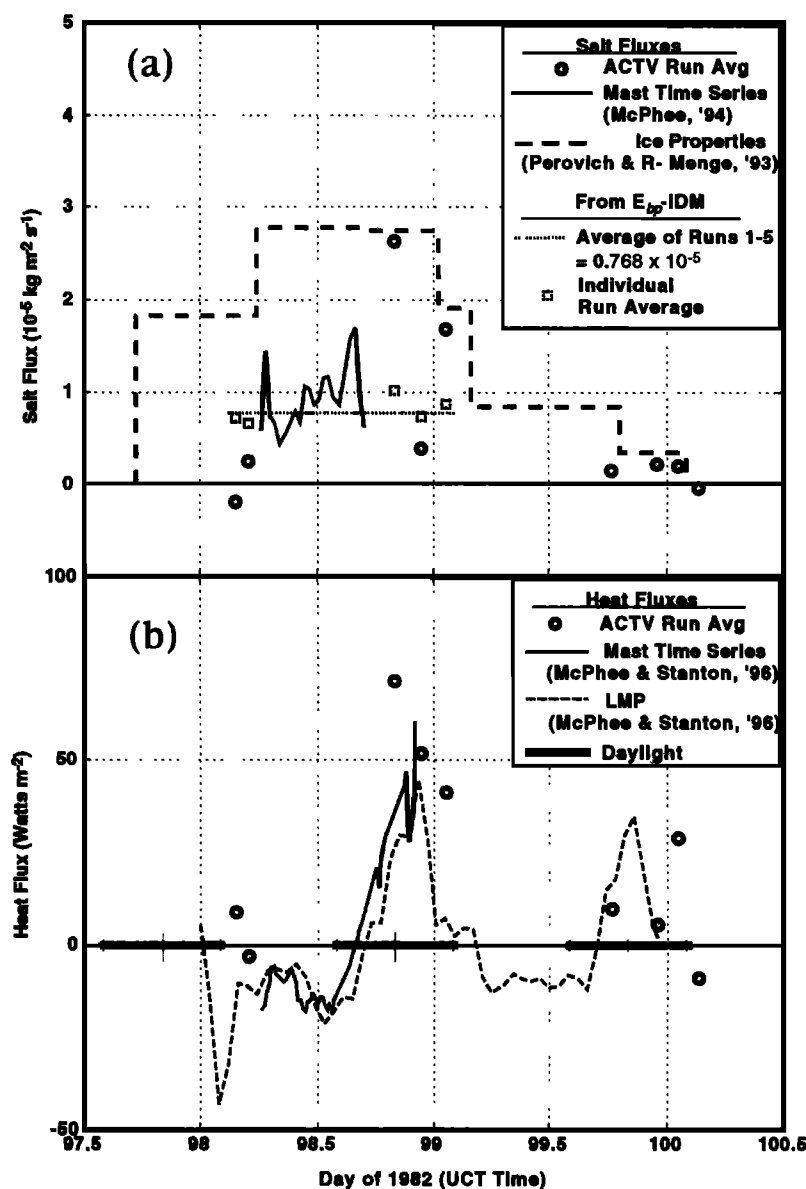


Figure 10. Downward (a) salt and (b) heat flux averages for all ACTV runs at lead 3 during LeadEx. Estimates by other means are also shown as described in the text. The estimates from the E_{bp} -IDM correspond to those of (7) in the text and Figure 7b.

turbulence is in the relative air velocity. Conversely, calculations suggest that the ACTV has so much surface area forward of the center of gravity that when it encounters an updraft, it has a tendency to pitch up and follow the updraft. Thus, with this static instability, the ACTV will tend to follow the updrafts and downdrafts with little relative vertical water velocity; the turbulence signal is in the motion of the ACTV. This tendency helps to counter inertia-induced effects as the ACTV first moves into an updraft or downdraft. The ACTV has some dynamic stability, so that once it moves vertically after the initial pitch change it will not continue to increasingly diverge in pitch. This tends to limit the ACTV vertical velocity to that of the water and limit the vertical excursions so as not to constantly trigger the vehicle control system. It would be advantageous to measure the water velocity relative to the ACTV, and in future vehicles we may do this. However, we think the dynamic factors cited above help explain the empir-

ical results illustrated in Figures 8, 9a, 9b, 9c, 10a, and 10b, which indicate that for the horizontal scales of lead convection the ACTV tends to follow the water motion, and the fluxes estimated using ACTV vertical velocity agree with the IDM fluxes and the fluxes measured by the fixed masts.

We analyzed individual runs at lead 3 in a variety of ways to determine spatial variability. Examination of salinity structure on adjacent legs of several runs convinced us that the individual plumes had no preferred orientation and were approximately of unit aspect ratio in the horizontal. We also tried overlaying results in several different coordinate systems, and we could find no preferred position for the plumes. We did find however that the energy tended to decrease beyond a certain point downstream of the edge. The picture is consistent with boundary layer turbulence modified by a change in surface flux.

Determining the spatial structure of the w 's from the ACTV data involves the same fundamental problem encoun-

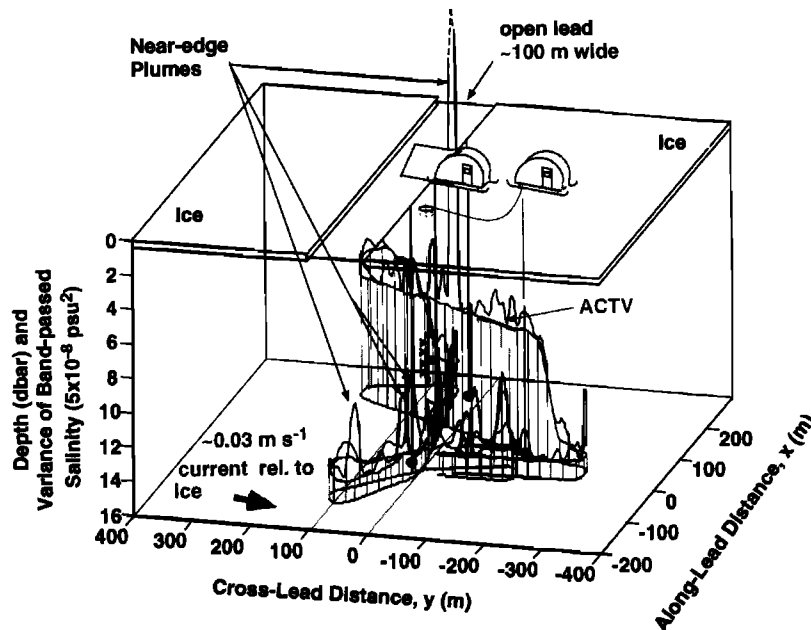


Figure 11. Lead 4 equipment setup and ACTV run 4 depth and variance of band-passed salinity in a perspective view. The arrangement of equipment was similar to that shown in Figure 2 for lead 3, but this figure is different from Figure 2 in that the run trajectory is projected on the lower surface and the vehicle depth is shown as the top of a curtain rising from the trajectory. The lead position is also projected on the lower surface. The variance of band-passed salinity is plotted relative to the depth curve.

tered when trying to determine time variation of flux at a point; the flux occurs in narrow (or short) intense bursts such as displayed by Figures 4 and 5. The Reynold's turbulent flux is by definition an ensemble average of the instantaneous flux over many independent realizations. In practice, time series of $w'S'$ are averaged over a suitable interval in order to approximate the ensemble average. It is assumed that there is a spectral gap such that the time variation of the overall process is much longer than the timescale of the turbulence. Here we are looking for spatial variability, and by analogy with the treatment of time series we must average over a suitable spatial scale. A composite average over several runs adds significance and an element of time averaging. For lead 3 data, composite averages of $w'S'$ in 1- or 2-m bins are extremely noisy, because the turbulent plumes are in different positions during each run. A high-resolution spatial composite is not feasible. However, averages over $2\pi\lambda$ (56 m) bins include roughly one turbulent plume per pass and provide reasonable results.

The composite average of $w'S'$ treated in this way for runs 1–5 is plotted along with the flux estimated by the E_{bp} -IDM in Figure 7b. Here the $2\pi\lambda$ bins are spaced a quarter bin apart. The average $w'S'$ over the whole area, $9.4 \times 10^{-6} \text{ kg m}^{-2} \text{ s}^{-1}$, has the most statistical significance and is very close to the average flux measured by McPhee [1994] at 4 m, $1 \times 10^{-5} \text{ kg m}^{-2} \text{ s}^{-1}$. It is 38% larger than the overall average of the E_{bp} -IDM flux, $6.8 \times 10^{-6} \text{ kg m}^{-2} \text{ s}^{-1}$. The average $w'S'$ under the lead away from the lead edge is about the same as the E_{bp} -IDM flux, and both methods indicate a marked decrease beyond about 75 m downstream. However, the $w'S'$ is elevated by a factor of 3 over the E_{bp} -IDM flux between the edge and 75 m downstream. This increased flux is heavily affected by a single very energetic plume observed slightly downstream of the edge during run 5 (D in Figure 5a). Thus we are uncertain about the magnitude of this maximum, but there

appears to be some intensification of the turbulence at 15 m within about 75 m downstream of the ice edge. Some implications of this will be discussed in the conclusions.

4. Convection Under a Lead With Little Ice Motion

4.1. Basic Observations

Lead 4 of LeadEx was much narrower than lead 3, and the ice motion was much less. The width of lead 4 varied over time from about 130 to 80 m (J. Bitters and E. D'Asaro, personal communication, 1992). As illustrated in the drawing of Figure 11, the average lead width was about 100 m, and the relative speed between the ice and the water was 0.03 to 0.04 m s^{-1} . Figure 12, taken from Figure 3 of McPhee and Stanton [1996], shows interesting differences in the character of the turbulence as well. Note that only here and in Figure 4, velocities and fluxes are positive upward. Figure 12 shows 1-hour records of vertical velocity, salinity, temperature, and salt and heat fluxes from the fixed sensors at the lead edge. The time records of velocity, temperature, and salinity are similar to those for lead 3 illustrated in Figure 4, with peaks every 8–10 min. However, with the average horizontal velocity of 0.03 m s^{-1} for this period, this implies a plume spacing of only about 16 m. This is typical for this lead; average spectra of mast-derived salinities weighted by wave number indicate a period of 9 min, and with an average relative velocity of 0.036 m s^{-1} , a plume spacing of 19.9 m. The mixed layer depth was about 30 m, so the plume spacing is substantially less than twice the mixed layer depth. Note also the relative absence of high-frequency texture in vertical velocity despite the shallow depth of the TIC. This indicates a lack of energetic, shear-driven turbulence near the surface. The heat and salt fluxes show a burst of three

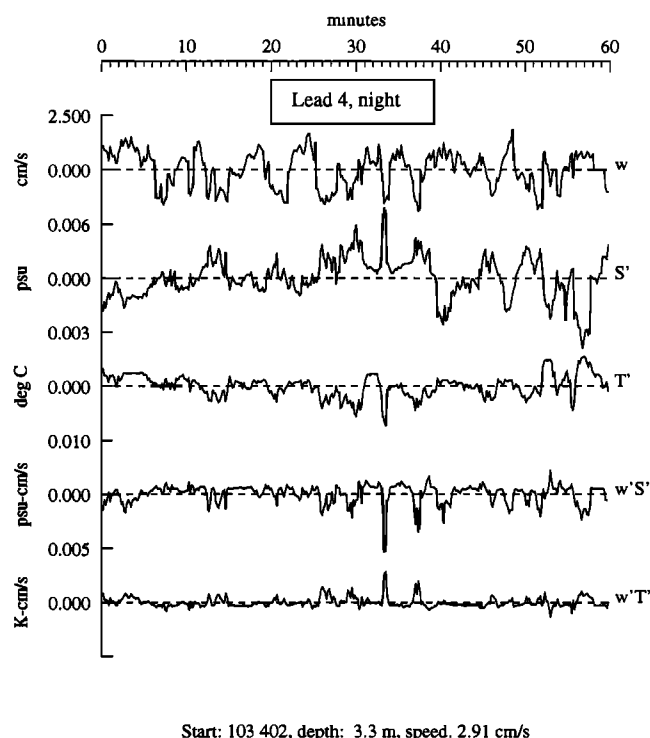


Figure 12. One-hour time series of mast-derived vertical velocity deviation, w' , salinity deviation, S' , and temperature deviation, T' , as in Figure 4 but during the night at lead 4. Also shown are the instantaneous salinity flux, $w'S'$, and heat flux, $w'T'$. For Figure 12 and Figure 4 the velocity and fluxes are positive upward. The convention for the other figures and the ACTV generally is that velocity and fluxes are positive downward. Average values of the fluxes are $\langle w'S' \rangle = -1.03 \times 10^{-5}$ psu m s $^{-1}$ and $\langle w'T' \rangle = 2.72 \times 10^{-6}$ K m s $^{-1}$ [from McPhee and Stanton, 1996].

or four plumes centered at about 33 min and weaker bursts at 12 and 55 min.

Considering mast-derived $w's'$ averaged, $\langle w's' \rangle$, for each of 16 independent 1-hour periods shows a division into a relatively high-flux group of 11 samples having an average downward flux of 5.8×10^{-6} psu m s $^{-1}$ and a low-flux group of 5 samples having an average downward flux of 2.5×10^{-6} psu m s $^{-1}$. The spectra weighted by frequency indicate a spectral peak at a 6.8-min period for the average of the low-flux cases and at a 8.9-min period for the high-flux cases. These are for an average relative velocity of 0.036 m s $^{-1}$ in both cases, so the $\langle w's' \rangle$ plume spacing is 15–20 m. There is some variation with salt flux magnitude, but the plume spacing is consistent with the spacing derived from salinity. So, while the turbulence at the lead edge looks familiar, it does not have the character of a forced convective boundary layer under the lead. The key differences from the lead 3 records are the decrease in fine-scale structure and the shorter distance between the convective plumes relative to the mixed layer depth.

The ACTV data from lead 4 present a different picture from that seen by the fixed sensors. Figure 13 shows vertical velocity, salinity, temperature, heat flux, and salt flux versus cross-lead distance for lead 4, ACTV run 2. There is a general salinity increase from the upstream edge to the downstream edge, followed by a decrease farther downstream. This salinity pattern is consistent with a surface flux of salt at the lead surface.

The dominant feature is the large (0.007 psu) salinity spike near the downstream lead edge (cross-lead distance = 0). There are two 0.002–0.003 psu salinity maxima at 40 and 70 m across the lead and two small (0.001 psu) broad maxima centered at –90 and –160 m. The pattern is suggestive of the model results of Smith and Morison [1993] that show convection to be concentrated in narrow plumes of high salinity at the edges of a wide lead, particularly the downstream edge. Similar features also appear in simulations of a narrower lead described by Smith and Morison [this issue]. The vertical velocity of Figure 13 indicates a 2–3 cm s $^{-1}$ downward (positive) plume at the downstream edge and smaller plumes spaced about 60 m apart downstream of the lead. There is a complex of smaller downward velocity plumes between 50 and 75 m across the lead. This is also consistent with Smith and Morison [1993, this issue], who find periodic pulsing of the dominant jets near the lead edges and occasional plumes forming in the middle of the lead. The salt flux is dominated by the downward plume near the downstream edge of the lead, with a small downward flux occurring near the upstream edge. Small downward and upward fluxes occur downstream at –75 to –140 m.

As shown by the salinity deviation measured during run 2 (Figure 13) and the variance of band-passed salinity during run 4 (Figure 11), there is significant activity tied to the lead geometry, with peaks in salinity and turbulence occurring near the lead edges. This relation between the convection pattern and the lead geometry is illustrated by a composite average of all crossings of the lead. Figures 14a and 14b show the averages of the salinity perturbation and the variance of the band-passed salinity versus cross-lead distance for all ACTV crossings of lead 4. The salinity perturbations and variance of band-passed salinity were calculated in the same way as for Figure 7. Figure 14a shows a trend of linearly increasing salinity across the lead in the downstream direction and a sharp drop in salinity beyond the downstream edge. The magnitude of the salinity variation across the lead is comparable to the larger variations at lead 3.

The variance of band-passed salinity in Figure 14b also shows an increase across the lead in the downstream direction. This is dominated by a strong peak at the downstream edge, with a broad maximum occurring in the middle of the lead and a small peak appearing at the upstream edge. The variance of band-passed salinity in the peak at the downstream edge is comparable to the maximum variances in Figure 10b for lead 3, but the average variance at lead 4 is about half that at lead 3. Downstream of lead 4, the variance is consistently low. Overall, the comparison with lead 3 is clear; the salinity fluctuations at lead 4 are about the same size but are more clearly confined to the lead. The variance of band-passed salinity, and presumably the turbulence, is less except in the downstream-edge plume. In general, the lead 4 pattern is more closely tied to the lead geometry.

4.2. Fluxes in the Free Convection Regime

The geometric constraint of convection at lead 4 results in a difference between the ACTV and fixed-mast measurements. This is seen clearly when we apply the inertial dissipation method of McPhee [this issue] to estimate the salinity flux. Following the work of McPhee [1994] and McPhee and Stanton [1996], McPhee [this issue] derives a method for determining the salt flux using the spectra of salinity alone in a free convection regime. For free convection the appropriate velocity scale of turbulence is $w_* = (\lambda \langle w'b' \rangle)^{1/3}$, where the buoy-

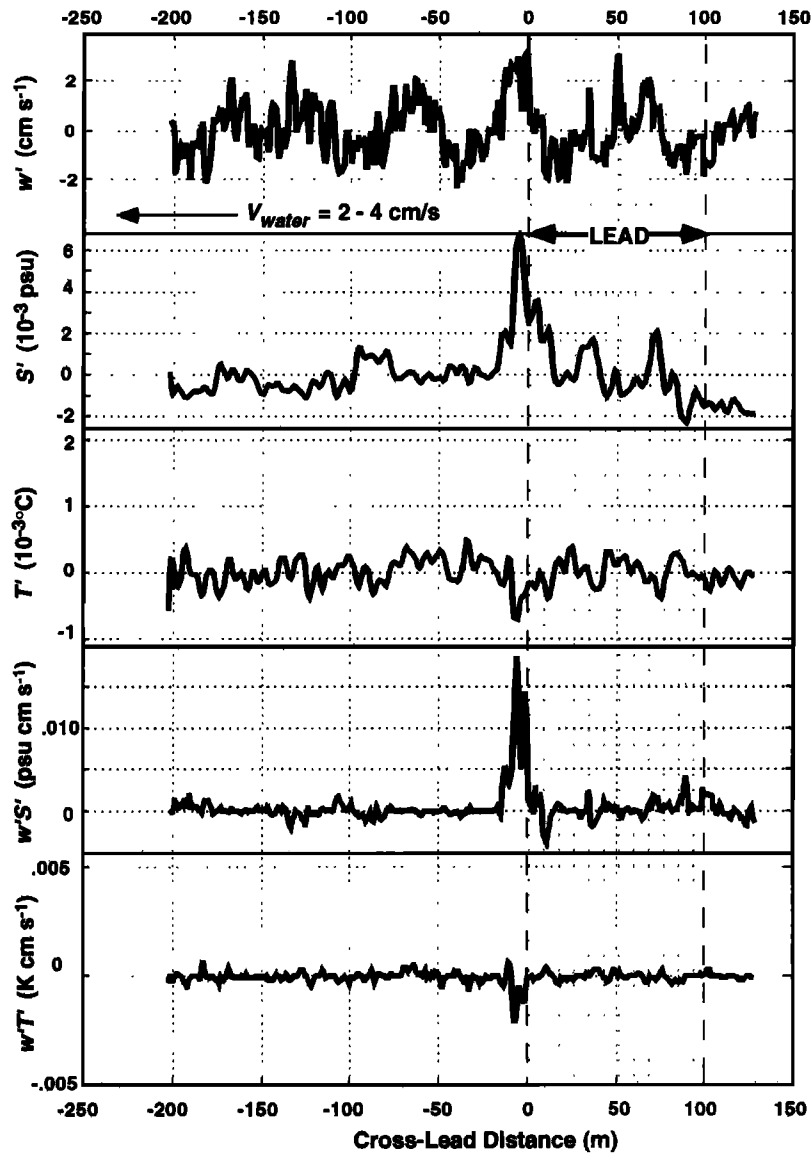


Figure 13. Vertical velocity, salinity, and temperature fluctuations and salt and heat fluxes versus cross-lead distance for ACTV run 2 at lead 4. The run was made at 9 m depth, 0516 UTC, April 12, 1992. Here w' and the fluxes are positive downward.

ancy flux, $\langle w'b' \rangle$, can be expressed here in terms of the salinity flux, $\langle w'S' \rangle = g\beta_s \langle w's' \rangle \rho^{-1}$, where g is the acceleration due to gravity, β_s is the linearized ratio of density change to salinity change, and ρ is the water density. Therefore the analog to (3) for dissipation of shear variance is

$$\left| \langle w'S' \rangle \frac{\partial S}{\partial z} \right| = \frac{\langle w'S' \rangle^2}{K} = \frac{|\langle w'S' \rangle|^{5/3}}{\lambda^{4/3} \left(\frac{\beta_s g}{\rho} \right)^{1/3}} = \varepsilon_s, \quad (8)$$

where $\partial S / \partial z$ is the vertical gradient of the mean salinity. Further, in the turbulent kinetic energy equation, the turbulent dissipation is driven by buoyant production, so the analog to (2) is

$$-\langle w'b' \rangle = -\frac{g}{\rho} \beta_s \langle w'S' \rangle = \varepsilon. \quad (9)$$

McPhee [this issue] solves (8), (9), and (4) iteratively. They can be combined to yield

$$|\langle w'S' \rangle| = \frac{\lambda}{\alpha_s^{3/4}} \left(\frac{g\beta_s}{\rho} \right)^{1/2} S_{ss}^{3/4} k^{5/4}. \quad (10)$$

As we did to obtain (7), we can divide the variance of band-passed salinity, E_{bp} , by the width of the pass band (0.4 rad m^{-1}) to get an effective spectral density at 1 rad m^{-1} . For $\rho = 10^3 \text{ kg m}^{-3}$, $g = 9.8 \text{ m s}^{-2}$, and $\beta_s = 0.8 \text{ kg m}^{-3} (\text{kg}_{\text{salt}} \text{ m}^{-3})^{-1}$,

$$|\langle w'S' \rangle| = 0.179 \lambda E_{bp}^{3/4}. \quad (11)$$

McPhee [this issue] uses the weighted (by k) salinity spectrum at the edge of lead 4 to estimate $\lambda = 2.8 \text{ m}$. Using (10), *McPhee* [this issue] obtained a salinity flux of $5.6 \times 10^{-6} \text{ kg m}^{-2} \text{ s}^{-1}$, in excellent agreement with direct $\langle w'S' \rangle$ calculations.

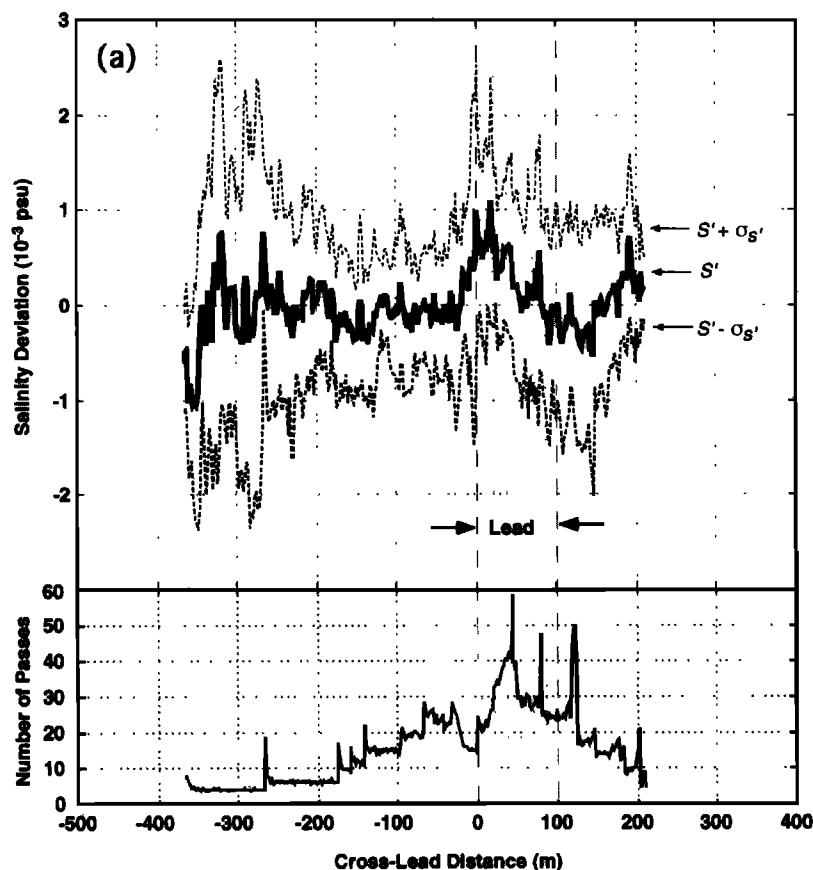


Figure 14a. (top) Composite average of salinity deviation versus cross-lead distance for all ACTV runs (1–8) at lead 4. The salinity deviation for each ACTV run is calculated as described in the text for Figure 7a. Here the results for all runs are collected in 2-m bins of cross-lead distance, and (bottom) the equivalent number of ACTV passes through each bin is shown. Only bins for which there are the equivalent of at least three ACTV passes are plotted.

Equation (11) is an amazingly compact relation. It indicates that in free convection it is necessary to know only the variance of band-passed salinity and the turbulent length scale in order to estimate the salt flux. In horizontally homogeneous, free convection bounded by a pycnocline, the convective cells fill the unstratified layer and have approximately unit aspect ratio. We saw such a case at lead 3, where the boundary layer was fully developed, and the convective plumes were spaced on average about two mixed layer depths, $2d$, apart. As a consequence of this geometry, the length scale goes as the dominant plume spacing divided by 2π , or $\lambda = d/\pi$. This is roughly comparable to the mixed layer multiplied by von Karman's constant, as surmised empirically by *McPhee* [1994]. With this value of the turbulent length scale, only the variance of band-passed salinity is needed to estimate the salt flux.

For lead 4, (11) would allow us to compute salt flux with only ACTV salinity measurements but for the difficulty of determining λ . The problem is that conditions at lead 4 were not horizontally homogeneous. At lead 3, where conditions were more nearly uniform, the horizontal wave number spectra from the mast and ACTV data agree (Figure 6a), and it is possible to estimate λ from ACTV spectra alone. At lead 4 the weighted salinity spectra from the ACTV data are much less energetic than the mast-derived spectra and do not show the distinctive peak used to determine λ . There are two reasons for this. First, the turbulent energies at the ACTV run depths were

lower under most of the lead and surrounding ice than at the downstream edge where the mast was located (Figure 14b). Second, λ varied across the lead and beyond because the convection had a persistent spatial pattern. In other words, the turbulence characteristics were not statistically stationary over an ACTV run track at lead 4.

Given the problems of horizontal inhomogeneity, we must make an assumption about the turbulent length scale in order to relate salt flux to the variance of band-passed salinity. The length scale, λ , must vary across the lead. The maximum value, 2.8 m, was measured at the downstream edge. Near the upstream edge and under the surrounding ice there is no buoyancy flux, and the length scale must be smaller given the weak relative current. A rough estimate of the background neutral turbulent length scale using *McPhee's* [1994] equation (15) and a typical U_i/u_* ratio for pack ice yields a value of $\lambda = 0.5$ m. We assume here that λ ramps up from 0.5 m at the upstream edge to 2.8 m at the downstream edge and then drops back to 0.5 m over a distance of $2\pi\lambda = 18$ m. The assumed λ is illustrated in Figure 14b (middle). With this assumption the variance of band-passed salinity of Figure 14b yields the salt flux estimate also shown in Figure 14b. The flux estimate based on the band-passed ACTV salinity agrees well with the mast-measured flux at the downstream edge. The turbulent salt flux is greatly enhanced near the downstream edge, being a factor

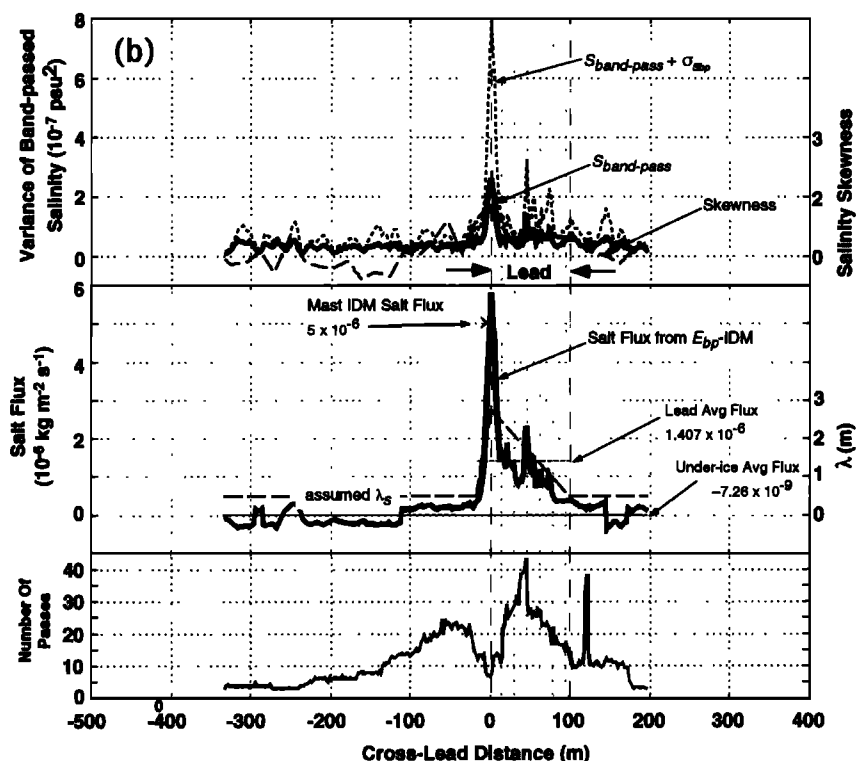


Figure 14b. Composite average of the variance of salinity band-passed at 1 rad m^{-1} for all ACTV runs (1–8) at lead 4. (top) The average plus 1 standard deviation and the skewness of the salinity perturbation are also shown. (middle) The salt flux estimated using the E_{BP} -IDM method of (11) as described in the text, along with the assumed value of λ and the salt flux obtained from the mast data, is shown. Positive salt flux is downward. As in Figure 14a, the results for all runs are collected here in 2-m bins of cross-lead distance (skewness is collected in 18-m bins), and (bottom) the equivalent number of ACTV passes through each 2-m bin is shown. Only bins for which there are the equivalent of at least three ACTV passes are plotted. Also, the variance of band-passed salinity measured during turns is not used.

of 4 greater than the lead average and a factor of 28 greater than the flux away from the lead.

The composite of Figure 14 is compelling because it shows such a persistent trend over all the runs. However, the details of the spatial structure of the salinity flux in the lead are revealed more clearly by averaging only the portions of runs 2–6 at depths less than 9.5 m. These do not cover as great a distance upstream and downstream of the lead, but they constitute most of the legs that transited both the upstream and downstream edges. Thus they give good snapshots of the spatial structure in the lead. Three different composite averages of S' , w' , and $w'S'$ for these runs are plotted versus cross-lead distance in Figure 15. The profiles were edited to remove w' excursions that were obviously commanded by the ACTV control system near turns and programmed depth changes. An additional salinity composite from profiles not edited for w' is also shown to expand the spatial coverage. The first composite average is in 1-m bins. This is shown in part to illustrate that the salinity flux does not have the usual high wave number, high variance characteristic of such measurements in a turbulent boundary layer. This is so because at lead 4 the energetic plumes tend to occur at around the same position near the downstream edge and to some extent near the upstream edge in a quasi-stationary pattern.

The S' , w' , and $w'S'$ averaged in $2\pi\lambda$ bins are shown, and though the peak amplitudes are less, the pattern is similar to

the higher-resolution profiles. The ratios of the means to the standard deviations in the $2\pi\lambda$ bins are measures of the quasi-stationary nature of the plumes. The average ratio for lead 3 is about 0.2. This is also typical for lead 4 away from the edges, but near the edges of lead 4 the ratio of bin average to bin standard deviation is typically 0.4. The $2\pi\lambda$ bin averages show the characteristic increase in salinity across the lead with a 1×10^{-3} psu peak at the downstream edge and a small peak about two thirds of the way across the lead. The average w' has broad peaks of about 0.005 m s^{-1} immediately downstream of both edges. The flux shows a dominant $2.4 \times 10^{-5} \text{ kg m}^{-2} \text{ s}^{-1}$ peak at the downstream edge and a $0.7 \times 10^{-5} \text{ kg m}^{-2} \text{ s}^{-1}$ peak near the upstream edge. The average flux from $2\pi\lambda$ downstream to across the lead is $6 \times 10^{-6} \text{ kg m}^{-2} \text{ s}^{-1}$.

To produce a composite picture that illustrates the instantaneous shape of the downstream-edge plume at high resolution, we have averaged the runs in 1-m bins after aligning the positions of their downstream-edge plumes. They have been aligned by shifting them in y such that the salinity maximum within 25 m of the downstream edge is positioned at $y = 0$. Figure 15 shows the S' , w' , and $w'S'$ averaged in this way. The true position of the salinity maximum is indicated in the small table in Figure 15. The average position is 4.6 m upstream of the lead edge, with a standard deviation of 7.8 m. Aligning the profiles by the downstream-edge salinity peak increases the velocity and flux peaks near both lead edges as

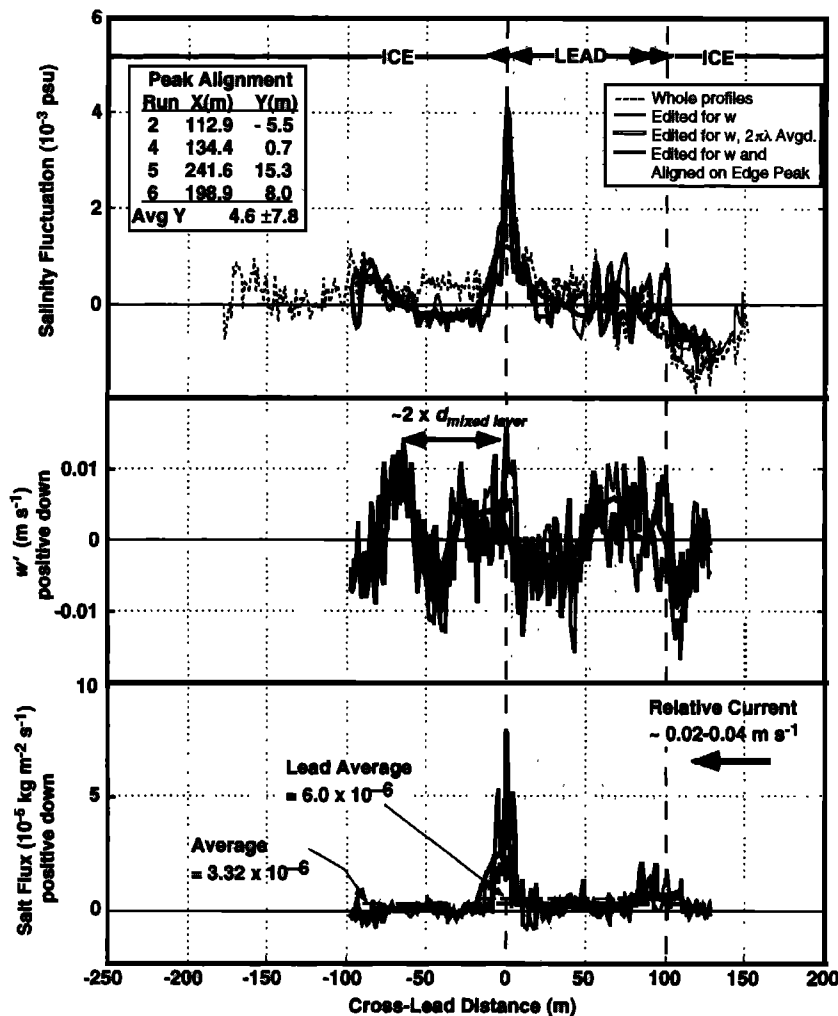


Figure 15. Composites of S' , w' , and $w'S'$ at 9 m depth measured with the ACTV during runs 2, 4, 5, and 6 under lead 4. Three types of profiles are shown. These have been collected in 1-m bins, collected in $2\pi\lambda$ (18-m) bins, and collected in 1-m bins after alignment to put the ice-edge salinity peak at $y = 0$. A salinity composite from profiles unedited for w' is also shown. For the composites aligned at the lead-edge salinity peak the table in Figure 15 shows the variation in the position of the ice-edge plume.

well as the downstream-edge salinity peak; it is as if with this adjustment the picture of lead convection is brought into sharper focus. The aligned salinity profiles indicate that the peak at the downstream edge is typically about 0.004 psu in magnitude and 25 m wide. The w' profile shows a 0.01 m s^{-1} peak at the lead edge flanked by a similar peak about 60 m downstream and a peak at about 80 m upstream (~ 20 m downstream from the upstream edge). Both the plume at the lead edge and the plume under the lead show a sharp upstream edge and a more slowly changing downstream edge. The salt flux is dominated by the plume at the downstream edge, which has a peak amplitude of $7.5 \times 10^{-5} \text{ kg m}^{-2} \text{ s}^{-1}$. A flux of 1.5×10^{-5} to $2.0 \times 10^{-5} \text{ kg m}^{-2} \text{ s}^{-1}$ is associated with the plume at the upstream edge. The upstream-edge salt-flux plume is associated with a combination of upward motion of less saline water right at the edge of the ice and downward motion of more saline water 10–20 m downstream.

The individual profiles making up the composites show significant variations in amplitude, as do time series measured near the lead edge. However, Figure 15 demonstrates that the convection pattern has a quasi-stationary character that in-

volves a plume and a strong flux close to the downstream edge. The E_{bp} -IDM results for the same runs used in Figure 15 are very similar to the results in Figure 14b for all runs, though the amplitudes average 20% greater. However, the $2\pi\lambda$ bin average flux, $w'S'$, computed directly from w' and S' is 4 times larger than the turbulent flux from the same runs estimated by E_{bp} -IDM. As will be discussed below, this reinforces the idea that quasi-stationary cellular convection, rather than boundary layer turbulence, dominates the salt flux at 9 m under lead 4.

5. Comparisons of Rapidly and Slowly Moving Leads

5.1. Forced Versus Free Convection

In many ways, lead 3 and lead 4 give two different views of lead convection, but there are also some interesting similarities. The differences between the two are typified by the relative importance of the lead-caused density disturbance and the background, shear-driven turbulence in controlling the circulation around the lead. Morison *et al.* [1992] express this as the

ratio, L_o , of the pressure gradient to the shear stress terms in the mean momentum equation,

$$L_o = \frac{g\beta_s F_s d}{\rho C_d U_i^3}, \quad (12)$$

where the mixed layer depth, d , is 30 m at both leads, and F_s is the salt flux at the lead surface. Morison *et al.* [1992] and Kantha [1995] also give similar nondimensional numbers that characterize the ratio of convectively driven and shear-driven turbulence in the lead. This formulation is used here partly because it is in terms of variables that are readily measured or predicted in large-scale models and partly for comparison with historical lead data summarized in Morison *et al.* [1992].

For lead 3 the maximum salt flux estimate from ice properties is about $3 \times 10^{-5} \text{ kg m}^{-3}$, and the flux estimated by our measurements is about $1 \times 10^{-5} \text{ kg m}^{-3}$. For these values, L_o at lead 3 ranges from 0.32, which is slightly into forced convection regime, to 0.96, which is mixed free and forced convection. The implication is that the lead 3 circulation may be thought of as a boundary layer strongly influenced by unstable buoyancy flux. This is born out by the observations. The ACTV and fixed sensors present a consistent picture of convection in a turbulent boundary layer. The convection is dominated by narrow, downward plumes spaced apart at twice the mixed layer depth. The plumes are carried downstream with the mean flow, so Taylor's hypothesis can be applied to the fixed-sensor data. They then agree with the ACTV horizontal profiles. We attempted to examine the spatial structure of the individual plumes observed with the ACTV and determined that individually, they were unit aspect ratio in the horizontal, had no apparent preferred orientation, and were not fixed to the lead geometry. The turbulence decreases far downstream of the lead, but this is consistent with the behavior of a boundary layer downstream of a change in surface buoyancy flux and roughness. The only unusual aspect in this picture is the apparent enhancement of turbulence near the lead edge. This will be discussed below.

That the lead 3 boundary layer is strongly influenced by the convection is born out by the results of McPhee and Stanton [1996], which show that shear production and buoyancy production contribute about equally in the turbulent kinetic energy equation. It can also be seen by looking at the profiles of Figure 4, which display both large-scale convective plumes and higher-frequency fluctuations due to shear production. The presence of the shear-generated and buoyancy-generated turbulence at high and low wave numbers, respectively, is also indicated by the flattening of the temperature and salinity spectra at high wave numbers in Figure 6a.

Estimating the salt flux from ice properties for lead 4 is difficult due to sampling problems and ice deformation. However, Perovich *et al.* [1995] indicate that the ice had grown to about 7 cm thickness after 16 hours. From this we can adjust the rate of ice formation and salt flux estimated for lead 3 to give representative values for lead 4. Depending on what we assume for the ice salinity, we get average salt flux estimates from $0.8 \times 10^{-5} \text{ kg m}^{-3}$ to $1.7 \times 10^{-5} \text{ kg m}^{-3}$. For these values we find L_o at lead 4 equal to 3.3 and 11.4, which are both in the free convection regime. The measurements support the notion that the circulation at lead 4 was dominated by convection. The basis of the IDM applied to lead 4 is that the turbulent velocity scale is the convective velocity scale w_* and that dissipation balances buoyant production. The method works very well in the fixed-mast data gathered at 4 m. The

ACTV data at 9 m indicate that the convective plumes vary with time, but as illustrated by Figure 15, the positions of the plumes are tied to lead geometry. The important features are the rising salinity across the lead and the dominance of narrow plumes at the downstream edge. Figure 15 also suggests a broader region of weak downward salt flux near the upstream edge. The w' and salinity sections indicate this upstream plume is actually due to an upward movement of low-salinity water at the upstream edge and downward movement of high-salinity water about 10–20 m into the lead. The quasi-stationarity of the pattern indicates it cannot be characterized as a boundary layer circulation.

5.2. Comparison of Temporal and Spatial Variations

Further aspects of the comparison between leads 3 and 4 are illustrated in Figure 16. It shows the composite flux profiles from the ACTV data plotted at the same vertical scale for both leads. It also shows sketches illustrating some important aspects of the lead dynamics and a table summarizing the average fluxes.

The temporal variations observed at the downstream edges of the two leads are very similar. This appears to be a coincidental result of spatial variability at lead 4. The low-frequency fluctuations in the time series at the edge of lead 4 (Figure 12) occur at about the same frequency as at lead 3. Spectral analysis of the mast salinity data indicates a characteristic period of 7–9 min, similar to the period at lead 3. At lead 3 this period translates into a spatial separation between convective plumes of 2 times the mixed layer depth, $2d = 60 \text{ m}$, but with the ice drift of $3\text{--}4 \text{ cm s}^{-1}$, at lead 4 this period translates into a spatial separation of only 15–19 m, substantially smaller than $2d$. Our hypothesis as to why the temporal variation should be the same at the two leads while the spatial variation is different is that the convection in lead 4 never develops vertically to the point where the mixed layer depth has an effect. At the upstream edge of a lead the convection will not extend to a significant depth. We expect that as the convection cells move downstream with the ambient current, they penetrate deeper. What is the effective depth of penetration at the downstream edge? We are guided by our experience at lead 3. There McPhee [1994] finds $\lambda = 9 \text{ m}$ and $2\pi\lambda = 56 \text{ m}$, or about 2 times the mixed layer depth. Our explanation is that the convection in the surface layer behaves as if it were limited to a depth of $\pi\lambda$ ($\pi \times 2.8 = 9 \text{ m}$ at lead 4), and the plumes will be spaced $2\pi\lambda$ (18 m) apart whether the convective boundary layer has grown down to the mixed layer depth or not. Thus, at the downstream edge of lead 4, we expect the period to be $2\pi\lambda/U_i = (17.6/0.036) \text{ s} = 8.1 \text{ min}$ roughly as observed.

We can complete the argument by noting that the rate at which the convection pattern grows should scale roughly with w_* . In deriving the convection IDM method for lead 4, McPhee [this issue] finds that w_* at the downstream edge is 0.0049 m s^{-1} . We have also hypothesized that λ varies from 2.8 m at the downstream edge to 0.5 m at the upstream edge. With the assumption that the flux is constant at the surface, w_* varies as the cube root of λ . Thus w_* at the downstream edge times $(0.5/2.8)^{1/3}$ yields $w_* = 0.0028 \text{ m s}^{-1}$ at the upstream edge. On average we might expect the depth of penetration to grow at an average of 0.0038 m s^{-1} . Thus the effective mixed layer depth at the downstream edge, after the water passes under the full width, L , of the lead, will be $\langle w_* \rangle L/U_i = 10.6 \text{ m}$. This is close to $\pi\lambda$ (9 m) and would produce a period of oscillation of 10 min in rough agreement with the observed

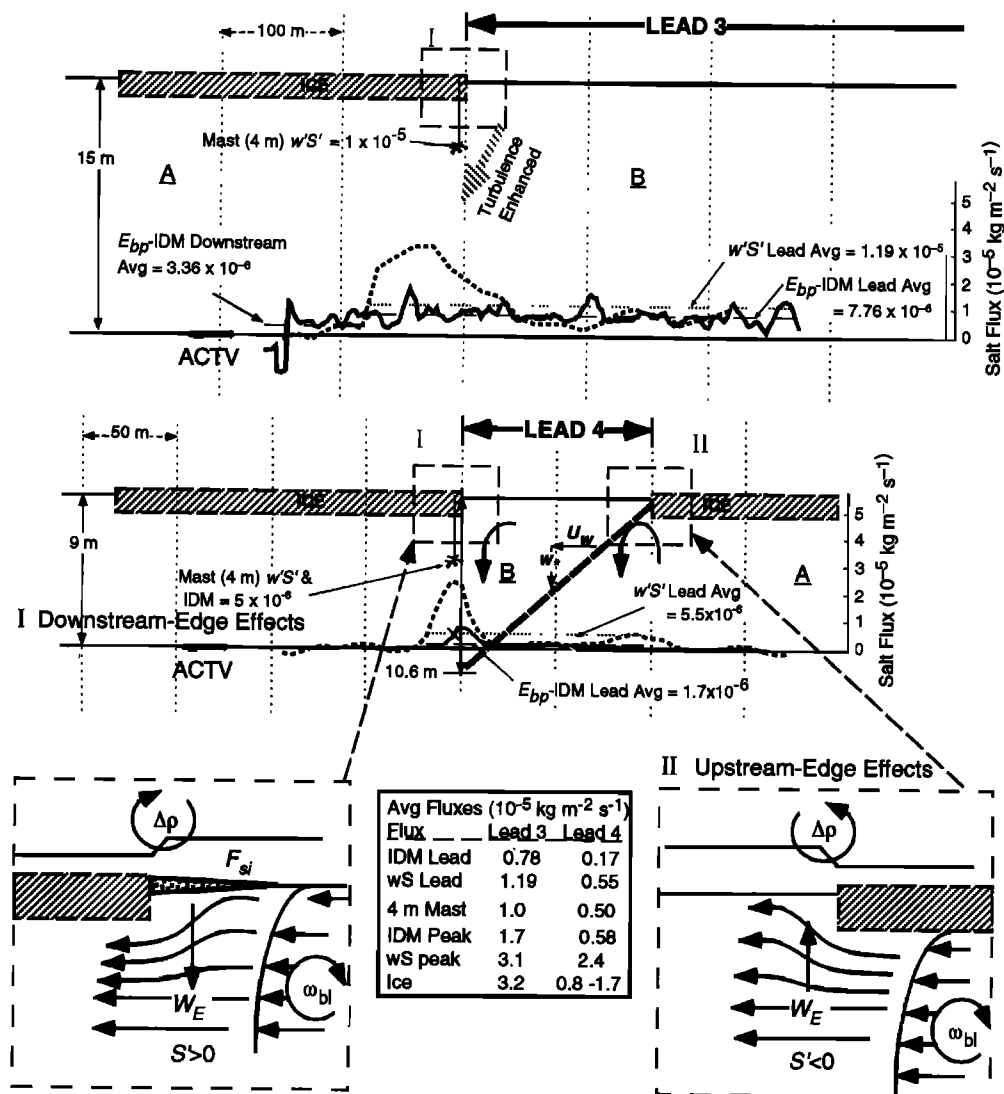


Figure 16. Schematics summarizing key features of convection observed at leads 3 and 4. The salt flux pattern for each lead is drawn to the same vertical scale, with the vertical axis origin at a position scaled to the ACTV run depth. Salt flux from direct $w'S'$ is indicated by a solid black line, and the flux from the E_{bp-IDM} is indicated by a dashed black line. The lead 4 E_{bp-IDM} flux used here is for the same data used for $w'S'$ here and in Figure 15. Factors affecting the convection near the lead edges are shown in the blowups. These are (1) the balance between the boundary layer vorticity, ω_{bl} , and the change in density at the edge, $\Delta\rho$, (moving flame effect), (2) the vertical velocity boundary condition due to flow around the ice edge, w_E , and (3) ice deformation at the downstream edge, F_{si} .

period. This suggests a pattern of convective boundary layer growth depicted by the dashed, gray line in the lead 4 sketch of Figure 16. The line extends downward and downstream with a slope = w_*/U_i from the upstream edge. In the region B above the line, convective turbulent conditions exist. In the region A below the line, the turbulence is largely a remnant of conditions upstream of the lead.

The spatial variation described above explains some of the other peculiarities of the flux results at lead 4. The table of average fluxes in Figure 16 shows that at each lead the $w'S'$ averaged under the lead and through a short active region downstream is close to the average flux measured at 4 m with the fixed mast. At lead 3 the average E_{bp-IDM} flux under the lead also is comparable to the mast average. This is because the mast, ACTV $w'S'$, and E_{bp-IDM} fluxes are all being mea-

sured in the same turbulent boundary layer. Lead 3 was so wide that the boundary layer filled the mixed layer over most of the lead width. Thus the steady state balance between production and dissipation assumed for IDM was well satisfied.

The situation for lead 4 is different. There the average ACTV- $w'S'$ and mast- $w'S'$ and mast-IDM fluxes agree, but the average E_{bp-IDM} flux is smaller by a factor of 3. This is because, as shown by the sketch of Figure 16, the ACTV was not in the boundary layer region, B, except near the downstream edge. There near the edge the E_{bp-IDM} flux rises to a value similar to the mast average (see Figures 14b and 16). Essentially, the salt moves downward by the action of smaller-scale turbulence in region B. Some is also advected slowly downstream. The mast- $w'S'$ and mast-IDM, being measured at 4 m near the downstream edge, see the turbulence charac-

teristic of the surface forcing over much of the lead width, and the average fluxes from the mast reflect the average surface forcing. Near the boundary between B and A, more of the flux is carried by the larger-scale quasi-stationary plumes comprising the lead scale circulation. This is the flux measured by the ACTV- $w'S'$ method. The ACTV- $w'S'$ measures the fluctuating and constant (about 10%) but nearly stationary plumes without any assumptions about the turbulent energy balance. Also, the ACTV's horizontal sections constitute a control volume boundary. Therefore ACTV- $w'S'$ gives a reasonable average flux, even if portions of the path are in the turbulence-dominated wedge near the surface or the relatively less turbulent region below the wedge. The E_{bp} -IDM method does not equal the ACTV- $w'S'$ flux in the upstream- and downstream-edge plumes at 9 m because the plumes are so narrow and intermittent that the steady state balance between buoyancy production and dissipation does not apply at the same scales as in the boundary region B. Actually, even in region B, near the downstream edge where λ is 2.8 m, using the variance of salinity band-passed at 1 rad m^{-1} may be problematic, though it seems to agree with the mast-IDM there.

At both leads the ACTV $w'S'$ profiles show increased activity near the edges. The near-edge activity is particularly important at lead 4 where it is the dominate source of flux at 9 m. The $w'S'$ composite peak at the downstream lead edge of lead 4 is 4 to 5 times the average flux (Figures 14b and 16). The existence of narrow, intense intermittent plumes near the downstream edge, as well as upstream-edge plumes for low ice velocities, is predicted by the two-dimensional model of *Smith and Morison* [1993, this issue]. The simulations of *Kantha* [1995] for conditions representative of lead 4 also imply a strong downward salt flux centered near the downstream edge, though *Kantha's* plume is spread over a wider region and is not intermittent. There are at least three important factors that give rise to the formation of lead-edge plumes or enhance turbulence near the lead edges. These are illustrated schematically in Figure 16.

In the model of *Smith and Morison* [1993] the edge plumes are associated with along-edge horizontal vorticity at the edges forced by the surface density contrast ($\Delta\rho$ in the Edge Effects panels of Figure 16) across the edges. At the downstream edge this vorticity is reinforced by the boundary layer vorticity, thus enhancing the strength of the downstream-edge plume. At the upstream edge, boundary layer vorticity is in the sense opposite to $\Delta\rho$, so the upstream plume tends to be smaller. This phenomenon has been observed by P. Rhines (personal communication, 1992) in laboratory and numerical simulations of a moving heat source. He refers to it as the "moving flame effect."

An additional factor, which we do not think has been studied, is that for a lead bordered by thick ice as at lead 4, there should be a tendency for upward near-surface motion at the upstream edge where water flows from under the thick ice up under the thin ice of the lead. The upward motion will carry relatively low salinity water. This and a downward motion of salty water slightly farther downstream will both result in downward salt flux in the manner we observe in Figures 13 and 15. Conversely, at the downstream edge, there is a requirement for downward motion from under the thin ice in the lead to under the neighboring thick ice. This motion carries more saline water from under the lead and results in downward salt flux. These edge motions, w_E in Figure 16, will be confined to within several ice thicknesses of the thick ice at the edge, but

they may be a substantial fraction of the ice velocity. Thus they provide a surface boundary condition that may trigger edge plumes, especially when ice velocity is high.

Finally, the tendency for stronger plumes at the downstream edge may be enhanced by increased salt flux due to ice deformation. On the second day of the deployment at lead 4, ice stalactites associated with rafting at the downstream edge were observed emitting brine [*Perovich et al.*, 1995]. *Perovich et al.* [1995] estimate about a 60% enhancement of salt flux in a band several meters wide next to the edge. This would certainly enhance the downstream-edge plume. However, it should also be noted that the strongest downstream-edge salinity plume was observed on run 2, prior to any rafting. Also, the flux maximum near the upstream edge cannot be explained in terms of deformation at the downstream edge. Although stalactites and extensive rafting were not observed at lead 3, it is possible that the desalinization of the ice near the edge was enhanced by horizontal stresses on the ice. Ice deformation near the downstream edge has been cited by D. Perovich (personal communication, 1996) as one possible reason why the flux estimates from ice properties are higher than the average fluxes measured in the ocean. (The other possibility is that snow blowing onto the lead surface may have made the ice growth and desalinization appear too great and produced erroneously high flux estimates.)

At lead 4 the ice velocity was so low that the w_E effect may have been relatively small. However, the cross-edge density gradient and the edge-plume circulation it causes are an inherent part of the lead circulation. Ice deformation is an added factor that enhances the downstream-edge plume. The resulting quasi-stationary edge plumes produce most of the salt flux at 9 m in the region that the smaller-scale convective turbulence does not reach.

Lead 3 is so wide and energetic that the boundary layer fills the mixed layer over most of the lead width, and edge plumes are not a defining characteristic of the lead circulation. However, the average flux observed at 15 m with the ACTV is also elevated at the edge and in a band immediately downstream, although the relative effect is not as great as at lead 4. All three edge effects may be important at lead 3, but the relatively high ice speed increases the possible importance the w_E effect. With a 0.1 m s^{-1} ice speed we can expect a region where w_E is of order 0.01 m s^{-1} near the edge. This is a substantial vertical velocity boundary condition, and along with the other mechanisms it will enhance the energy of convective plumes advecting past. At 15 m depth these may appear as energetic plumes as at D and C in Figure 15a.

5.3. The Importance of Lead Width

The overall impression left by the comparison of the lead 3 and lead 4 observations is that though lead 3 can be characterized as forced, boundary layer, convection and lead 4 demonstrated the quasi-stationary circulation features of free convection, each demonstrated characteristics of the opposite type. The mix of characteristics was especially important at lead 4. There the mix occurred partly because instability was more important than shear-driven turbulence as indicated by the lead number, L_o , and partly because the lead width was relatively small.

The results suggest lead width is important for two reasons. First, it is important in terms of development of the lead internal boundary layer (area B of Figure 16). In principal this may apply whether the internal boundary layer is due to a

change in surface buoyancy flux or surface roughness. It can be quantified in terms of the fraction, L_{LW} , of the lead width, L , required for the boundary layer to develop to full depth,

$$L_{LW} = \frac{dU_i}{V_* L}. \quad (13)$$

For the unstable case such as at lead 4 the turbulent velocity scale $V_* = w_* = (\lambda |w' b'|)^{1/3}$. For the fully developed, salt-flux-driven, convective boundary layer, $\lambda = d/\pi$, and the ratio is

$$L_{LWC} = \frac{dU_i}{\left(\frac{dg\beta_s F_s}{\pi\rho}\right)^{1/3} L} = \frac{U_i}{L} \left(\frac{\pi\rho d^2}{g\beta_s F_s}\right)^{1/3}. \quad (14)$$

For lead 4 this yields $L_{LWC} = 1.45$, so as we observed, the full convective boundary layer cannot develop under lead 4. A similar relation can be developed for a shear-driven boundary layer where the turbulent velocity scale is u_* . In such a case the boundary layer develops to a depth $0.4u_* f^{-1}$, and the ratio is $L_{LWS} = 0.4U_i(fL)^{-1}$. At lead 3, where mixed convective and shear-driven turbulence occurred, $L_{LWC} = 0.363$ and $L_{LWS} = 0.314$, so by either parameter the boundary layer was fully developed under most of the lead. In cases where these lead width parameters are greater than one we should expect a convection pattern with the quasi-stationary cells in the lower and upstream regions of the mixed layer under the lead.

The other important factor in the spatial pattern of lead convection must be the ratio of the lead width to the mixed layer depth, $L_{od} = L/d$. Assuming L_{LWC} is greater than 1 so that the quasi-stationary cells are important, the lead has to be wide enough for unit aspect ratio cells to develop in the mixed layer. Of course, we only examined lead 4, for which this ratio was over 3, but we speculate that if the ratio is less than 1, it is probably difficult for a coherent cell to form. A ratio of 2 is probably ideal for forming a downward plume at each lead edge. Greater ratios will result in various cell patterns. Taken together, these spatial scaling arguments suggest that many medium-sized leads will have at least a few quasi-stationary convective cells with an overlying convective boundary layer region. These leads will show a mix of characteristics between the boundary layer and cellular convection.

6. Conclusions

Finally, we comment on the implications of these observations, especially with regard to modeling them at a variety of scales. Parameterizing mixing in individual lead models is made difficult by the closeness of the lead scale to the turbulent scale. In the model of *Smith and Morison* [1993] the sub-grid-scale viscosity is limited to the neutral stability value upstream of the lead. The rationale for this was to let convective cells develop at as fine a scale as possible and predict the detailed features of the convection. *Kantha* [1995] used a higher-order closure [*Mellor and Yamada*, 1982] in his lead simulation. His model produces broader, steadier convection cells than the narrow intermittent plumes of *Smith and Morison* [1993]. *Kantha* argues that the turbulent diffusion of *Smith and Morison* [1993] is too weak and should be explicitly enhanced to account for unstable stratification. The model of *Kantha* [1995] produces results for lead 4 conditions that are more

static and somewhat broader than we observe, though it gives a good description of conditions averaged over a long period of time. The higher-order closure approach of *Kantha* [1995] should work well for boundary layer leads like lead 3. The *Smith and Morison* [1993] approach does a good job of illustrating the intermittent quasi-stationary plumes and enhanced edge effects such as those at lead 4. However, it may underestimate sub-grid-scale mixing in the near-surface layer.

The key modeling problem is to use a grid size and value of diffusion that are appropriate to the spatial structure of the features being simulated. For lead convection at medium size leads, where L_{LWC} is large and L_{od} is order 1, this is particularly difficult. The lead, the quasi-stationary cells, and the large-scale turbulence are all close to the same size. Furthermore, closure schemes derived on the basis of data from experiments in horizontally homogeneous conditions or with assumptions about horizontal homogeneity may not respond appropriately in regions where these conditions do not apply. In medium-sized leads the random turbulent motions and quasi-stationary circulation exist with overlapping scales, and conditions are far from homogeneous. Ideally, a model should use a grid size small enough to resolve the quasi-stationary features. These appear to scale with the mixed layer depth. Then only enough diffusion to account for the sub-grid-scale mixing should be used. This will let the model solve for the large, energy-containing eddies that make up much of the quasi-deterministic response. While the *Smith and Morison* [1993] model is a simple two-dimensional attempt at this, the best approach is probably to use a complete three-dimensional, large-eddy simulation such as that used by *Glendening* [1995] to model atmospheric lead convection.

A broad goal of lead convection research is to develop useful descriptions of the enhancement of mixing by localized, rapid freezing for large-scale, coupled air-sea-ice models. For the present it is unrealistic to contemplate resolving individual leads in such models; thus detailed physical process studies like the one described here must look for simplifying principles. This paper and its companion [*McPhee*, this issue], combined with earlier work, suggest such principles. First, the fixed-mast time series at the edges of the leads and the rapidly sampled ACTV horizontal profiles indicate that the dominant turbulent length scales (λ) are significantly larger than those found under thick ice with no buoyancy flux but appear to be limited to a fraction (of order $1/\pi$) of the mixed layer depth. This limiting scale is reached where leads are extensive enough for the turbulent flow to be fully adjusted to the surface flux conditions, and convective eddies fill the mixed layer. Our data also suggest that the downstream growth of the length scale may be expressed in terms of the ratio of w_*/U_i . The product of the dominant turbulent scale with the proper turbulent velocity scale is the eddy diffusivity in the mixed layer. There are two candidates for the scale velocity in statically unstable flows: u_* and w_* . At lead 3 they were approximately equal. At lead 4, w_* was significantly larger. Our results indicate that eddy diffusivity depends on whichever scale velocity is larger.

For a large-scale, coarse resolution model, one would hope that the effect of leads and thin ice on both surface buoyancy flux and upper ocean mixing would be approximately linear with area, so that their impact could be easily expressed, e.g., as a simple function of the ice-thickness distribution. The mixing length and scale velocity arguments developed here are especially amenable to such treatment. However, it is not clear that such linearity holds. For example, is the impact of a few

wide leads (like lead 3) equivalent to an equal area of many narrow leads (like lead 4) where the turbulent boundary layer may not be fully developed, and the fluxes are partly due to a cellular convection pattern? The usual way to apply a one-dimensional mixed layer model is to drive it with the area average momentum and salt flux. If this is done for the areal average flux from a collection of many slowly moving leads, the simulated mixed layer will mix, deepen, and become uniformly more saline due to enhanced turbulence. However, our results at lead 4 indicate that in such a case the salt rejected from the surfaces of the leads may be carried through the mixed layer in narrow intermittent plumes. The composite salinity profile of Figure 14a suggests that this does not increase the salinity of the upper mixed layer, and the saline water must settle to the base of the mixed layer. Contrary to what the one-dimensional mixed layer model would suggest, such slowly moving leads may stratify the mixed layer and make it more shallow by this convective process. Meaningful small-scale numerical models (i.e., compatible with the field observations) run with realistic lead and thin ice distributions could be of much help in finding ways to represent these perhaps paradoxical effects of leads in large-scale models.

Acknowledgments. This work was supported by ONR grants N00014-90-J-1077, N00014-96-1-0083, N00014-94-C-0023, and N00014-96-C-0032. We would like to thank Russ Light and Dan Stearns for their ability and hard work in building and operating the ACTV and Andy Heiberg, John Bitters, and the rest of the LeadEx logistics team for making LeadEx work.

References

- Fleury, M., and R. G. Lueck, Direct heat flux measurements using a towed vehicle, *J. Phys. Oceanogr.*, 24(4), 810–801, 1994.
- Glendening, J. W., Horizontally integrated atmospheric heat flux from an Arctic lead, *J. Geophys. Res.*, 100(C3), 4613–4620, 1995.
- Hinze, J. O., *Turbulence*, 2nd ed., 790 pp., McGraw-Hill, New York, 1975.
- Kantha, L. H., A numerical model of Arctic leads, *J. Geophys. Res.*, 100(C3), 4653–4672, 1995.
- Kozo, T. L., Initial model results for Arctic mixed layer circulation under a refreezing lead, *J. Geophys. Res.*, 88(C5), 2926–2934, 1983.
- LeadEx Group, The LeadEx Experiment, *Eos Trans. AGU*, 74(35), 393, 396–397, 1993.
- Light, R., and J. H. Morison, The autonomous conductivity-temperature vehicle: First in the SEASHUTTLE family of autonomous underwater vehicles for scientific payloads, in *Oceans '89 Conference Record*, pp. 793–798, IEEE Press, Piscataway, N. J., 1989.
- Maykut, G. A., Energy exchange over young sea ice in the central Arctic, *J. Geophys. Res.*, 83(C7), 3646–3658, 1978.
- McPhee, M. G., Turbulent heat flux in the upper ocean under sea ice, *J. Geophys. Res.*, 97(C4), 5365–5379, 1992.
- McPhee, M. G., On the turbulent mixing length in the oceanic boundary layer, *J. Phys. Oceanogr.*, 24(9), 2014–2031, 1994.
- McPhee, M. G., An inertial-dissipation method for estimating turbulent flux in buoyancy-driven, convective boundary layers, *J. Geophys. Res.*, this issue.
- McPhee, M. G., and T. P. Stanton, Turbulence in the statically unstable oceanic boundary layer under Arctic leads, *J. Geophys. Res.*, 101(C3), 6409–6428, 1996.
- Mellor, G. L., and T. Yamada, Development of a turbulent closure model for geophysical fluid problems, *Rev. Geophys.*, 20(4), 851–875, 1982.
- Morison, J., Physical oceanography instrumentation for the polar regions: A review, *IEEE J. Oceanic Eng.*, 14(2), 173–185, 1989.
- Morison, J. H., M. G. McPhee, T. B. Curtin, and C. A. Paulson, The oceanography of winter leads, *J. Geophys. Res.*, 97(C7), 11,199–11,218, 1992.
- Muench, R. D., D. C. Smith, and C. A. Paulson, Convection beneath freezing leads: New observations compared with numerical model results, *J. Geophys. Res.*, 100(C3), 4681–4692, 1995.
- Perovich, D. K., J. A. Richter-Menge, and J. H. Morison, The formation and morphology of ice stalactites observed under deforming lead ice, *J. Glaciol.*, 41(138), 305–312, 1995.
- Schaus, R. H., and J. A. Galt, A thermodynamic model of an Arctic lead, *Arctic*, 26, 208–221, 1973.
- Smith, D. C., IV, and J. H. Morison, A numerical study of haline convection beneath leads in sea ice, *J. Geophys. Res.*, 98(C6), 10,069–10,083, 1993.
- Smith, D. C., IV, and J. H. Morison, Nonhydrostatic haline convection under leads in sea ice, *J. Geophys. Res.*, this issue.
- Smith, J. D., Lead-driven convection in the Arctic Ocean (abstract), *Eos Trans. AGU*, 54, 1108–1109, 1973.
- Thorpe, S. A., M. Cure, and M. White, The skewness of temperature derivatives in oceanic boundary layers, *J. Phys. Oceanogr.*, 21(3), 428–433, 1991.
- M. G. McPhee, McPhee Research Company, 450 Clover Springs Road, Naches, WA 98937. (e-mail: miles@wolfenet.com)
- J. H. Morison, Polar Science Center, Applied Physics Laboratory, University of Washington, 1013 NE 40th Street, Seattle, WA 98105. (e-mail: morison@apl.washington.edu)

(Received August 20, 1996; revised June 4, 1997; accepted June 26, 1997.)